

Nanospintronics with carbon nanotubes

Audrey Cottet¹, Takis Kontos², Sangeeta Sahoo³, Hon Tin Man⁴, Mahn-Soo Choi⁵, Wolfgang Belzig⁶, Christoph Bruder³, Alberto Morpurgo⁴ and Christian Schönenberger³

¹Laboratoire de Physique des Solides, Bâtiment 510, Université Paris Sud 91405, Orsay Cedex, France

²Laboratoire Pierre Aigrain, Ecole Normale Supérieure, 24, rue Lhomond, 75231 Paris Cedex 05, France

³Institute of Physics, University of Basel, Klingelbergstr. 82, CH-4056 Basel, Switzerland

⁴Kavli Institute of NanoScience Delft, Faculty of Applied Sciences, Delft University of Technology, Lorentzweg 1, 2628 CJ Delft, The Netherlands

⁵Department of Physics, Korea University, Seoul 136-701, Korea

⁶Departement of Physics, University of Konstanz, M703, D-78457 Konstanz, Germany

E-mail: cottet@lps.u-psud.fr, kontos@lpa.ens.fr

Abstract. One of the actual challenges of spintronics is the realization of a spin-transistor allowing to control spin transport through an electrostatic gate. In this review, we report on different experiments which demonstrate a gate control of spin transport in a carbon nanotube connected to ferromagnetic leads. We also discuss some theoretical approaches which can be used to analyze spin transport in these systems. We emphasize the roles of the gate-tunable quasi-bound states inside the nanotube and the coherent spin-dependent scattering at the interfaces between the nanotube and its ferromagnetic contacts.

PACS numbers: 73.23.Fg, 73.63.Kv, 85.75.Hh

1. Introduction : nanospintronics

The quantum mechanical spin degree of freedom is now widely exploited to control current transport in electronic devices. For instance, the readout of magnetic hard disks is based on the spin-valve effect, i.e. the tunability of a conductance through the relative orientation of some ferromagnetic polarizations [1]. However, realizing spin injection in nanostructures, e.g. mesoscopic conductors or molecules, would allow to implement further functionalities. For example, the realization of a "spin-transistor" would allow an electric field control of the spin valve effect through an electrostatic gate [2,3]. In this context, carbon nanotubes are particularly interesting, because they should exhibit a long spin life time and can be contacted with ferromagnetic materials. In this review, we present the state of the art regarding the realization of spin-transistor-like devices with carbon nanotubes. In section 2, we introduce the basics of the spin-valve effect. In section 3, we present a theoretical description of spin-transport in quantum wires with ferromagnetic contacts. We put a special emphasis on the roles of the gate-tunable resonant states inside the wire and the coherent spin-dependent scattering at the boundaries of the wire. In section 4, we present the state of the art in contacting carbon nanotubes with ferromagnetic materials, and evoke different contact effects which could mimic spin-dependent transport phenomena. In section 5, we review different experiments which have demonstrated a gate control of spin-transport in carbon nanotubes so far. Eventually, we give some conclusions and perspectives in section 6.

2. The spin-valve geometry

The most standard method to inject or detect spins in an insulating or conducting element M is to use the spin-valve geometry [4, 5], in which M is connected to two ferromagnetic leads L and R (figure 1, left). One has to measure the conductances G^P and G^{AP} of the spin valve for lead magnetizations in the parallel (P) and antiparallel (AP) configurations. This requires to use two ferromagnets with different coercive fields (H_{cL} and H_{cR} respectively) for switching one magnetization with respect to the other with the help of an external magnetic field H (figure 1, right). The spin signal or magnetoresistance is then defined as the relative difference $MR = (G^P - G^{AP})/G^{AP}$.

Let us consider the situation in which the element placed between the two ferromagnetic contacts is a tunneling barrier with a transmission probability independent of energy [6]. This case, usually referred to as Jullière's model, describes the principle of magnetic memories and magnetic read heads. From Fermi's Golden rule, the transmission probability of the barrier for spins $\sigma \in \{\uparrow, \downarrow\}$ is proportional to the electronic densities of states at the Fermi energy $N_{l,\sigma} = N_l(1 + \sigma\eta_l p_l)$ for spins σ at both contacts, with $l \in \{L, R\}$ and $\eta_l \in \{+1, -1\}$ the direction of the magnetization at contact l . Here, N_l is the spin averaged density of states and p_l the spin polarization in contact l . The conductance G^P of the barrier in the parallel configuration is proportional to $N_L N_R [(1 + p_L)(1 + p_R) + (1 - p_L)(1 - p_R)]$ whereas the conductance G^{AP} in the anti-

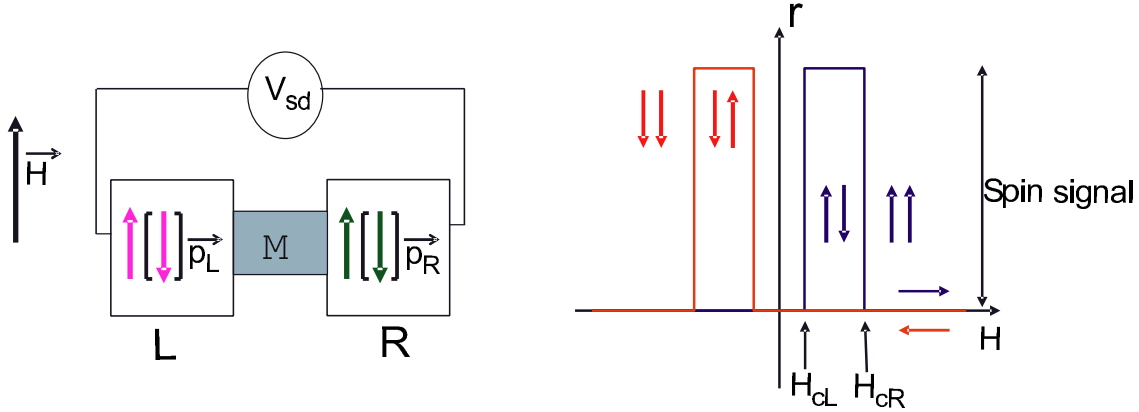


Figure 1. Left: Electrical diagram of a circuit with the spin-valve geometry. The element M is connected to two ferromagnetic leads L and R , in which the electronic density of states has magnetic polarizations \vec{p}_L and \vec{p}_R . The three elements in series form a spin-valve, which is voltage-biased with a source-drain voltage V_{sd} . A magnetic field \vec{H} is applied to the circuit. Right: Typical shape of the resistance curve $r(H)$ measured in the spin-valve while increasing (blue line) and then decreasing (red line) H . Since the two contacts L and R have different coercive fields H_{cL} and H_{cR} , it is possible to reverse selectively the directions of \vec{p}_L and \vec{p}_R during this cycle. This introduces an hysteretic pattern in the $r(H)$ curve, from which the value of the magnetoresistance $MR = (G^P - G^{AP})/G^{AP}$ of the spin-valve can be obtained. Here, one has $MR > 0$.

parallel configuration is proportional to $N_L N_R [(1 + p_L)(1 - p_R) + (1 - p_L)(1 + p_R)]$. This leads to

$$MR = \frac{2p_L p_R}{1 - p_L p_R}.$$

If the spin polarizations p_L and p_R have the same sign, the magnetoresistance of the device is positive because the current flowing in the antiparallel configuration is lower due to the imbalance between $N_{L,\sigma}$ and $N_{R,\sigma}$.

In the following, we consider the case in which element M is a carbon nanotube. In contrast with Jullière's model of a tunneling barrier, the transmission of the nanotube cannot be considered as constant with energy due to the existence of quasi-bound states between the two ferromagnetic contacts. Furthermore, it is possible to tune the energy of these bound states with an electrostatic gate. This significantly modifies the behavior of carbon-nanotube-based spin valves, as we are going to explain theoretically in the next section.

3. Spin transport in finite size quantum wires

Carbon nanotubes can display a large variety of behavior, depending on their intrinsic properties and on the characteristics of their electrical contacts. Even in the case of a clean nanotube (i.e. with no structural defects), electronic transport can occur in different regimes, depending on the transparency of the contacts. For high contact resistances $R > h/e^2$, a nanotube can behave as a quantum dot, in which Coulomb blockade determines the transport properties [7], whereas for low contact resistances

$R < h/e^2$, transport is mainly determined by quantum interference [8]. Here, we will mainly consider these two situations. For simplicity, we will model the nanotube as a one dimensional quantum wire.

3.1. Spin dependent transport in a non-interacting ballistic wire.

Although electron-electron interactions should be of primary importance in one dimensional quantum wires, it is instructive to consider first a non-interacting picture. In addition, as we will see in section 5, such a simplified picture captures the main features of some available experiments.

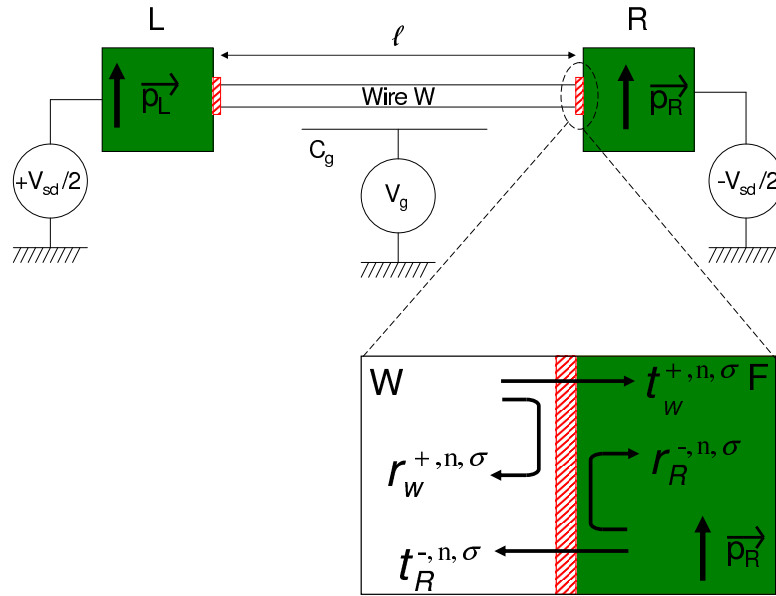


Figure 2. Electrical diagram of a ballistic wire w with length l connected to ferromagnetic leads L and R with magnetic polarizations \vec{p}_L and \vec{p}_R . The wire is voltage-biased with a source-drain voltage V_{sd} and capacitively coupled to a gate voltage source V_g . Inset: Scattering description of the interface between the wire and a contact. We use transmission and reflection amplitudes $t_l^{\epsilon,n,\sigma}$ and $r_l^{\epsilon,n,\sigma}$ for electrons with spin σ of transverse channel n , incident from element $l \in \{L, R, w\}$ with direction ϵ ($\epsilon = +$ for right-going incident electrons and $\epsilon = -$ for left-going incident electrons)

3.1.1. Transmission of a F-wire-F ballistic system We consider the circuit of figure 2, with W a non-interacting ballistic wire with length l contacted to two ferromagnetic leads L and R . In the non-interacting limit, electronic transport through this device can be described using a scattering approach [9]. As represented in the bottom inset of figure 2, this description involves complex amplitudes of transmission and reflection $t_l^{\epsilon,n,\sigma}$ and $r_l^{\epsilon,n,\sigma}$ for electrons with spin σ of transverse channel n , incident from element $l \in \{L, R, w\}$ with direction ϵ ($\epsilon = +$ for right-going incident electrons and $\epsilon = -$ for

left-going incident electrons). Assuming that the different channels n are not coupled by interfacial scattering, the behavior of the device only depends on the transmission probabilities $T_{L(R)}^{n,\sigma} = |t_{L(R)}^{+(-),n,\sigma}|^2$ and on the reflection phases $\varphi_L^{n,\sigma} = \arg(r_w^{-,n,\sigma})$ and $\varphi_R^{n,\sigma} = \arg(r_w^{+,n,\sigma})$ at the side of the wire. Indeed, the conductance of the circuit in configuration $P[AP]$ can be calculated from the expression

$$G^{P[AP]} = G_Q \sum_{n,\sigma} \int_{-\infty}^{+\infty} \mathbb{T}_{P[AP]}^{n,\sigma}(E) (-\partial f(E)/\partial E) \quad (1)$$

where $f(E) = [1 + \exp(E/k_b T)]^{-1}$ is the Fermi-Dirac distribution and where

$$\mathbb{T}_{P[AP]}^{n,\sigma} = \frac{T_L^{n,\sigma} T_R^{n,\sigma}}{|1 - [(1 - T_L^{n,\sigma})(1 - T_R^{n,\sigma})]^{1/2} e^{i(\varphi_L^{n,\sigma} + \varphi_R^{n,\sigma} + 2\delta_0 + \sigma\gamma_H^n)}|^2} \quad (2)$$

is the probability that an electron of channel n with spin σ coming from lead $L(R)$ is transmitted to lead $R(L)$. Here, we have introduced the orbital phase $\delta_0 = \ell k_{Fw}^n(V_g)$ acquired by an electron upon crossing the wire once and $\gamma_H^n = g\mu_B H \ell / \hbar v_{Fw}^n$, with H the external magnetic field. We call $k_{Fw}^n(V_g)$ the gate-dependent wave vector of electrons of channel n inside the wire, $v_{Fw}^n(V_g)$ the corresponding Fermi velocity, g the Landé factor and μ_B the Bohr magneton. The denominator of equation (2) accounts for the existence of resonant states which are due to multiple reflections between the two contacts. These resonances lead to peaks in the $G^{P[AP]}(V_g)$ curves. In the case of ferromagnetic contacts, the interfacial scattering properties depend on spin and on the configuration $c \in \{P, AP\}$ of the ferromagnetic electrodes (we omit the index c in $T_{L(R)}^{n,\sigma}$ and $\varphi_{L(R)}^{n,\sigma}$ for brevity). In the following, we investigate the effects of a finite spin polarization of the tunneling rates $P_l^n \neq 0$, and of a *Spin-Dependence* of Interfacial Phase Shifts (SDIPS), i.e. $\Delta\varphi_l^n \neq 0$, with

$$\begin{aligned} T_l^{n,\sigma} &= T_l^n (1 + \eta_l \sigma P_l^n) \\ \varphi_l^{n,\sigma} &= \varphi_l^n + \eta_l \sigma \frac{\Delta\varphi_l^n}{2}. \end{aligned}$$

for $l \in \{L, R\}$. Here, $\eta_l \in \{+1, -1\}$ denotes the direction of the magnetization at contact l .

The quantum wires which we have in mind are carbon nanotubes. Two different types of carbon nanotubes can be fabricated: Single-Wall Nanotubes (SWNTs) and Multi-Wall Nanotubes (MWNTs). A SWNT consists of a single graphene sheet that is rolled up into a cylinder. A MWNT consists of a set of coaxially stacked graphene cylinders. In the case of a SWNT, it is possible to have only two channels involved in current transport at low voltages (the energy levels of SWNTs often display a twofold degeneracy related to the K-K' degeneracy of the energy bands of graphene [10, 11]). Assuming two identical channels with no coupling, the behavior of such a nanotube can be understood from the study of a one-channel quantum wire, which is presented in section 3.1.2 (the conductance of the nanotube will be twice that of the single-channel quantum wire and the magnetoresistance will be identical). For MWNTs, more channels are generally involved in the low voltage electronic transport. We will thus present in section 3.1.3 the case of a quantum wire with several channels.

3.1.2. Single channel case In this section, we omit the channel index n . We assume that the gate voltage V_g induces a shift of the wire electrostatic potential which is small compared the Fermi energy of the wire, i.e. $\alpha V_g \ll E_{Fw}$, where $\alpha = C_g/C_\Sigma$ is the ratio between the gate capacitance and the total capacitance of the wire. In this limit, one finds $\delta_0 = \ell k_{Fw} + (e\alpha V_g - E_{Fw})(\pi N_{Fw}/2)$ where $N_{Fw} = 2\ell/\pi\hbar v_{Fw}$ is the density of states in the wire, and k_{Fw} and v_{Fw} are the Fermi wavevector and velocity in the wire. Therefore, the resonant peaks in the $G^{P[AP]}(V_g)$ curve correspond to the cancelation of resonant energies of the form

$$E_{P[AP]}^{\sigma,j} = (2\pi j - \varphi_L^\sigma - \varphi_R^\sigma - \sigma\gamma_H)(\hbar v_{Fw}/2\ell) - e\alpha V_g, \quad (3)$$

with $j \in \mathbb{Z}$.

Magnetoresistance of a 1-channel wire with no SDIPS In this paragraph, we investigate the behavior of the wire for $\Delta\varphi_i^n = 0$, and thus define resonant energies $E^j = E_{P[AP]}^{\uparrow,j} = E_{P[AP]}^{\downarrow,j}$ for $\gamma_H = 0$. From equation (3), the resonant peaks in the conductance curves are spaced by $\Delta E = E^{j+1} - E^j = \hbar v_{Fw}/2\ell$ which is usually called the intrinsic level spacing of the wire. Figure 4 shows with black dashed lines the conductance $G^P(V_g)$ and the magnetoresistance $MR(V_g)$ of a one-channel wire. For convenience, we have plot the physical quantities as a function of δ_0 instead of the gate voltage V_g . The conductance shows resonances with a π -periodicity in δ_0 , corresponding to the intrinsic level spacing ΔE . Strikingly, the magnetoresistance can become negative for certain values of V_g which correspond to a resonance in G^P . This is in contrast with the early Jullière's model evoked in section 2. In order to understand this situation (see figure 3), it is convenient to consider the limit of low transmissions $T_l \ll 1$, in which one can expand $\mathbb{T}_{P[AP]}^\sigma$ around $E = E^j$ (see [9]) to obtain a Breit-Wigner-like formula [12]

$$\mathbb{T}_{P[AP]}^\sigma = \frac{T_L^\sigma T_R^\sigma}{(\pi N_{Fw}[E - E^j])^2 + (T_L^\sigma + T_R^\sigma)^2/4} \quad (4)$$

Off resonance, i.e. when $(E - E^j)^2 \gg (T_L^\sigma + T_R^\sigma)/\pi N_{Fw}$, the transmission probability $\mathbb{T}_{P[AP]}^\sigma$ of the contact for electrons with spin σ is proportional to $T_L^\sigma T_R^\sigma$. This leads to

$$MR = \frac{2P_L P_R}{1 - P_L P_R}$$

like in Jullière's model. At resonance, i.e. when $E = E^j$, the situation is different. We will consider for simplicity the very asymmetric case $T_L^\sigma \ll T_R^\sigma$. In this case, equation (4) gives $\mathbb{T}_{P[AP]}^\sigma = 4T_L^\sigma/T_R^\sigma$, which leads to

$$MR = -\frac{2P_L P_R}{1 + P_L P_R}$$

Thus, it appears clearly that the change of sign in the MR signal is a direct consequence of the existence of quasi-bound states in the wire.

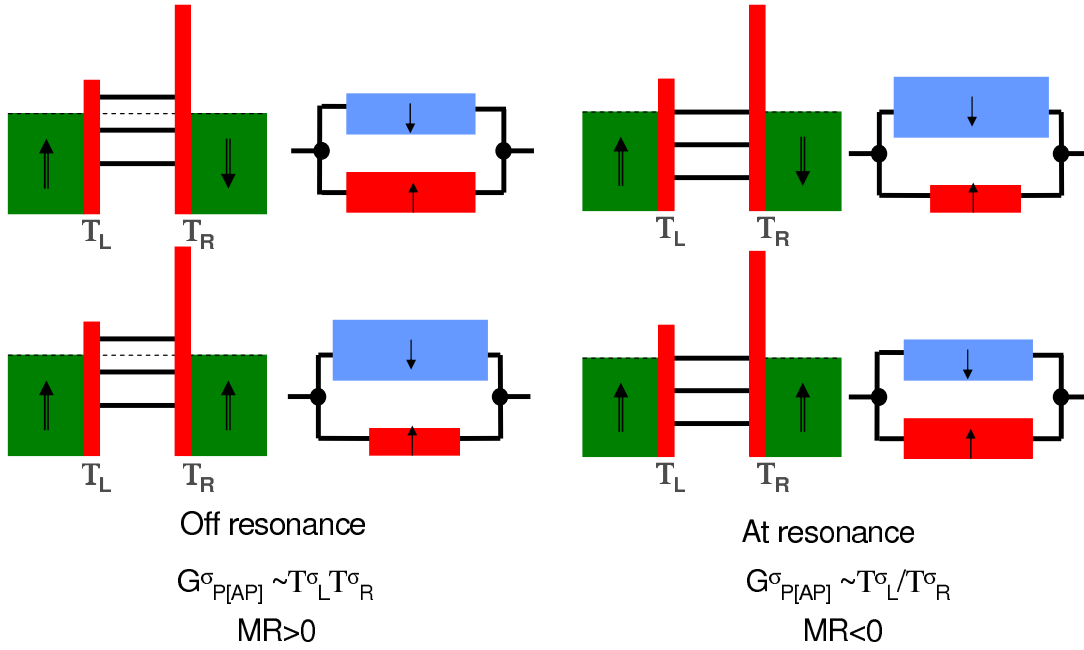


Figure 3. Picture of the resonant tunneling mechanism for very asymmetric barriers. Here, we assume $T_L^{\sigma} \ll T_R^{\sigma}$ and $P_L = P_R$. A bigger resistance element represents a higher resistance value. Off resonance (left panels), the transmission probability $\mathbb{T}_{P[AP]}^{\sigma}$ of the circuit for spins σ scales with $T_L^{\sigma} T_R^{\sigma}$ in the $P[AP]$ configuration. This leads to a positive MR like in Jullière’s model. On resonance (right panels), $\mathbb{T}_{P[AP]}^{\sigma}$ scales with $4T_L^{\sigma} / T_R^{\sigma}$, which leads to a negative MR .

Role of the Spin Dependence of Interfacial Phase Shifts (SDIPS). So far, we have assumed that the interfacial reflection phases of electrons of channel n coming from the wire were spin-independent, i.e. $\varphi_l^{\uparrow} = \varphi_l^{\downarrow}$ for $l \in \{L, R\}$. Nevertheless, the interface between a ferromagnet and a non-magnetic material can scatter electrons with spin parallel or antiparallel to the magnetization of the ferromagnet with different phase shifts, because electrons are affected by a spin-dependent scattering potential at this interface. This *Spin-Dependence* of Interfacial Phase Shifts (SDIPS) can modify significantly the behavior of many different types of mesoscopic circuits, like diffusive ferromagnetic/normal/ferromagnetic spin valves [13], superconducting/ferromagnetic hybrid circuits [14], Coulomb blockade systems [15, 16] and Luttinger liquids [17]. Reference [18] has shown that non-interacting ballistic wires can also be affected by the SDIPS. From equation (3), in case of a finite SDIPS, the resonant energies of the 1-channel wire are spin-dependent. This allows to define an SDIPS-induced effective

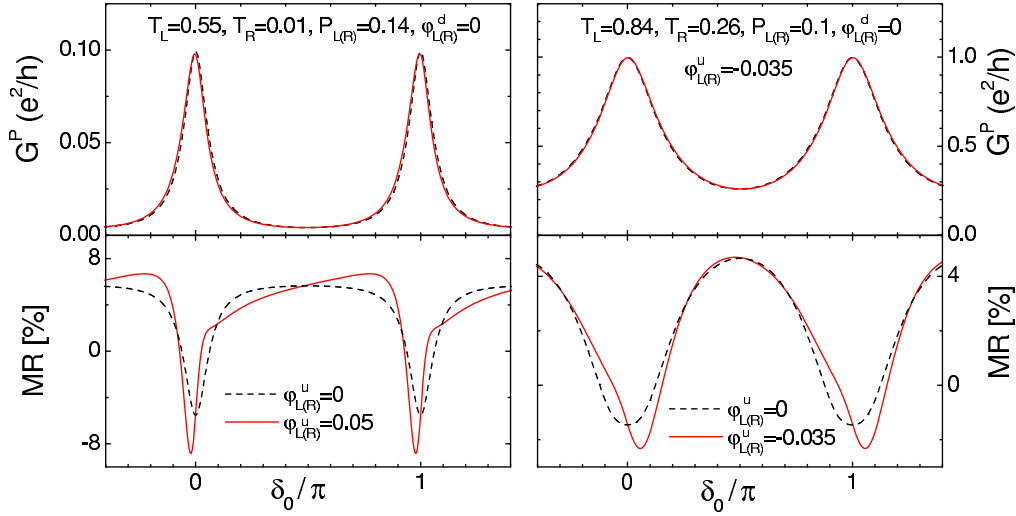


Figure 4. Linear conductance G^P (top panels) and magnetoresistance MR (bottom panels) for a single channel wire, as a function of the spin-averaged phase δ_0 acquired by electrons upon crossing the wire (δ_0 is linear with V_g in the limit considered here, see text). We show the results in case of no SDIPS (black dashed lines) and for a value of SDIPS finite but not resolvable in the conductance curves (red full lines). The left and right panels correspond to two different sets of parameters. When the contacts have no SDIPS, the oscillations in $MR(\delta_0)$ are symmetric. A low SDIPS ($|\Delta\varphi^{P[AP]}| \lesssim T_L + T_R$) can be detected qualitatively in the $MR(\delta_0)$ curves because it breaks the symmetry of these oscillations. In sections 5.2.1 and 5.2.3, we will compare these theoretical results with measurements done in SWNTs connected to PdNi contacts.

field h_{SDIPS}^c such that

$$E_c^{\downarrow,j} - E_c^{\uparrow,j} = g\mu_B h_{SDIPS}^c = \frac{\eta_L \Delta\varphi_L + \eta_R \Delta\varphi_R}{\pi N_{Fw}}$$

for $c \in \{P, AP\}$. Importantly, this effective field is configuration-dependent. For instance, in the case of symmetric barriers, one has $\Delta\varphi_L = \Delta\varphi_R$, thus h_{SDIPS}^P can be finite in the parallel case, but h_{SDIPS}^{AP} must vanish in the antiparallel case due to the symmetry of the problem.

The effects of the effective field h_{SDIPS}^c will depend on its amplitude. Let us first imagine that the SDIPS effective field is very strong in the parallel case, i.e. $|\Delta\varphi_L + \Delta\varphi_R| \gtrsim T_L + T_R$, and that the barriers are symmetric, leading to $h_{SDIPS}^{AP} = 0$ (one can imagine to obtain this situation by fabricating a symmetric device with strongly spin-dependent barriers, by using e.g. ferromagnetic insulators evaporated between the wire and the metallic contacts). From equation (2), this would allow to resolve the level spin-splitting $g\mu_B h_{SDIPS}^P$ in the conductance curve $G^P(V_g)$, and thus to obtain a shift of the conductance peaks from the P to the AP configurations. A giant MR effect with a sign tunable with V_g would thus be obtained. This illustrates that a strong SDIPS would be very useful for realizing an efficient control of spin-dependent transport in nanowires. Nevertheless, since the appropriate device fabrication has not been achieved yet, we refer the reader to reference [18] for the detailed study of the effects of a strong SDIPS and focus here on the case of a weaker SDIPS. It is possible that a weak SDIPS

occurs in actual experiments. Indeed, when a standard ferromagnetic contact material is evaporated directly on a wire, the interfacial scattering potential which affects the electrons can already depend on spin.

Figure 4, red full lines, shows the conductance $G^P(V_g)$ (top panels) and the magnetoresistance $MR(V_g)$ (bottom panels) for a device with a weak SDIPS. Although the SDIPS-induced spin-splitting is too weak to be resolved in the conductance curves for the parameters used here, it modifies qualitatively the spin-valve behavior of the device. Indeed, when there is no SDIPS, from equation (2), the $MR(V_g)$ oscillations are always symmetric with V_g . This symmetry is broken by the SDIPS. This is due to the fact that, in the presence of a weak SDIPS, the position of the global maximum corresponding to $E_c^{\uparrow,j}$ and $E_c^{\downarrow,j}$ is different for $c = P$ and $c = AP$. This effect provides a qualitative way to detect the presence of a finite SDIPS in the circuit.

3.1.3. Multichannel case. For MWNTs, it is usually assumed that transport occurs mainly through the outer shell [19]. However, since the diameter of MWNTs is larger than that of SWNTs, the spacing between the 1D subbands of the outer shell is lower [20]. As a consequence, a multichannel description is *a priori* needed if one wants to account for the MR . We have evaluated the conductance and the MR from equations (1) and (2), for a MWNT with two ferromagnetic contacts. In the simple case where there is no subband mixing, one can determine the transmission $\mathbb{T}_{P[AP]}^{n,\sigma}(E)$ occurring in these equations via the wave vector $k_{Fw}^n(V_g) = k_{Fw} + \sqrt{(e\alpha V_g - E_{Fw})^2 / (\hbar v_{Fw})^2 - n^2 / R_{nt}^2}$, where R_{nt} is the radius of the MWNT [21]. For a radius $R_{nt} = 2.7nm$, the subband spacing amounts to $\sim 180meV$. As the Fermi energy shift of MWNTs due to surface adsorbates can be as high as $\sim 1eV$ [22], up to 6 subbands can contribute to charge and spin transport. We have thus taken into account 6 subbands in the calculation. Figure 5 shows the calculated conductance G^P (top panel) and the magnetoresistance MR (bottom panel) for $T = 0$ (black full lines) and $T = 1.85$ K (dashed red lines). We have used contact parameters $P_{L(R)} = 0.2$, $T_L = 0.45$ and $T_R = 0.04$ for all the channels and a coupling $\alpha = 0.01$. For simplicity, we have assumed no SDIPS. At $T = 0$, the conductance shows peaks which correspond to the resonant states in the different channels. Due to the larger number of channels, the intrinsic energy spacing between these resonances is reduced. As a result of the combination of the different conducting channels, beatings occur for certain regions of gate voltage. Importantly, the MR can become negative, for the same reason as in the one channel case. At $T = 1.85$ K, it is not possible anymore to resolve the single level resonances. Due to thermal averaging, the conductance and magnetoresistance are roughly determined by the envelop of the transmissions. Therefore, the magnetoresistance shows approximately periodic sign changes with a period which is much larger than the intrinsic energy spacing between the resonant states. This type of behavior will be illustrated with measurements performed with MWNTs in section 5.2.2.

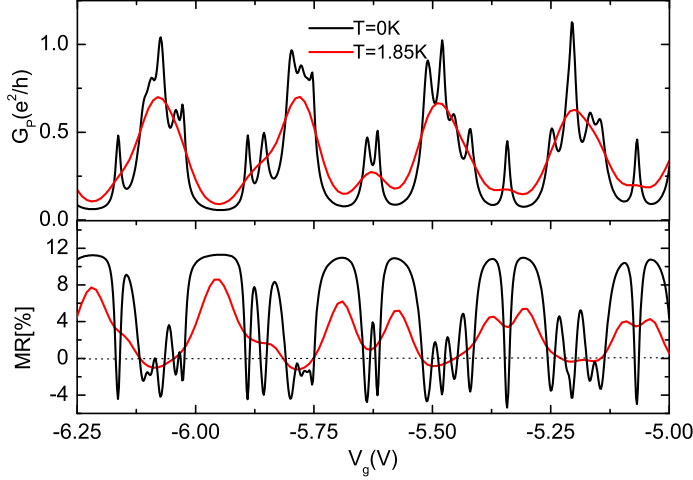


Figure 5. Conductance G^P (top panel) and magnetoresistance MR (bottom panel) calculated for a MWNT with two ferromagnetic contacts, for $T = 0$ (black lines) and $T = 1.85$ K (red lines). We have assumed that current transport occurs through 6 independent channels. We have used $P_{L(R)} = 0.2$, $T_L = 0.45$, $T_R = 0.04$ and $\alpha = 0.01$ for all channels. A radius of $R_{nt} = 2.7$ nm and a Fermi level of $E_w^F = 1$ eV have been used for the nanotube in order to calculate the wavevector $k_{F_w}^n$ associated to channel $n \in \{1..6\}$. Beatings occur in the zero temperature signals, due to the combination of the different channels. Therefore, at $T = 1.85$ K, the MR signal seem to oscillate with a period which is much larger than the intrinsic spacing between the resonant levels.

3.2. Spin dependent transport in a quantum dot.

The tunnel junctions connecting the ferromagnetic leads to the nanotubes have often a small capacitance of the order of 10 aF. In such a case, at low temperatures ($T < 10$ K), a finite charging energy $U = e^2/C_\Sigma$ is required to add electrons on a nanotube. The interplay of Coulomb blockade and spin dependent transport phenomena have attracted a lot of theoretical and experimental interest recently (see for instance [15, 23–28]). We introduce below a very recent theoretical development [16] which allows to address spin transport in the Coulomb blockade regime corresponding to experiment [29].

We assume that strong Coulomb interactions are added to the wire of figure 2, so that we have a quantum dot connected to ferromagnetic leads. In the interacting regime, the scattering approach used in the former section is not suitable anymore for describing this system. One can adopt a description based on the Anderson-like hamiltonian

$$H = H_{dot} + H_{leads} + H_c$$

with

$$H_{dot} = \sum_{d,\sigma} \xi_{d\sigma} c_{d\sigma}^\dagger c_{d\sigma} + \sum_{d,d',\sigma,\sigma' [(d,\sigma) \neq (d',\sigma')]} \frac{U}{2} n_{d\sigma} n_{d'\sigma'} \quad (5)$$

$$H_{leads} = \sum_{k,\sigma} \xi_{k\sigma} c_{k\sigma}^\dagger c_{k\sigma} \quad (6)$$

$$H_c = \sum_{d,k,\sigma} \left(t_{d\sigma}^k c_{d\sigma}^\dagger c_{k\sigma} + (t_{d\sigma}^k)^* c_{k\sigma}^\dagger c_{d\sigma} \right) \quad (7)$$

Here, $\xi_{d\sigma}$ refers to the energy of the dot orbital state d for spin σ , $\xi_{k\sigma}$ to the energy of lead state k for spin σ and $t_{d\sigma}^k$ is an hopping matrix element. The index k runs over the electronic states of lead L and R . We assume that the spin σ is preserved upon tunneling, like in section 3.1. Coulomb interactions are taken into account through the term in U , with $n_{d\sigma} = c_{d\sigma}^\dagger c_{d\sigma}$.

Although the notion of interfacial scattering phase is less natural here than with the scattering approach of section 3.1, it is possible to take into account the effects related to the SDIPS in the present interacting model. Indeed, by construction of hamiltonian (5), for $U = 0$, each orbital level $\xi_{d\sigma}$ corresponds to a resonant level $E_c^{\sigma,j}$ of section 3.1, with $\xi_{d\downarrow} - \xi_{d\uparrow} = g\mu_B h_{SDIPS}^c$. One can therefore introduce the effective Zeeman splitting h_{SDIPS}^c in equation (5) as a generalization of the SDIPS concept to the interacting case. This can be justified physically on the following basis. In the non-interacting case, we have considered that the ferromagnetic exchange field leads to a spin-dependent interfacial potential, responsible for the spin-dependent scattering. For a double barrier system, the ferromagnetic exchange field makes the confinement potential of electrons on the dot spin-dependent as well. This naturally induces a spin-dependence of the orbital energies, which is the counterpart of the spin-splitting of the resonant energies found in section 3.1.

In the interacting case, the zero-bias conductance of the circuit can be expressed as [30]

$$\frac{h}{e^2} \frac{G^c}{2} = \sum_{d,\sigma} \int_{-\infty}^{+\infty} d\omega \frac{\partial f(\hbar\omega)}{\partial \omega} \frac{\Gamma_{d\sigma}^L(\hbar\omega)\Gamma_{d\sigma}^R(\hbar\omega)}{\Gamma_{d\sigma}^L(\hbar\omega) + \Gamma_{d\sigma}^R(\hbar\omega)} \Im m[G_{d\sigma}(\omega)] \quad (8)$$

with, for $l \in \{L, R\}$, $\Gamma_{d\sigma}^l(\xi) = \sum_k 2\pi |t_{d\sigma}^k|^2 \delta(\xi - \xi_{k\sigma})$, and $G_{d\sigma}(\omega) = \int_{-\infty}^{+\infty} G_{d\sigma}(t) e^{i\omega t} dt$ with $G_{d\sigma}(t) = -i\theta(t) \left\langle \left\{ c_{d\sigma}(t), c_{d\sigma}^\dagger(0) \right\} \right\rangle$. For comparison with the experimental data of reference [29], one has to study current transport in the limit in which the width of conductance peaks displayed by the circuit is not limited only by temperature but also by the tunnel rates ($k_B T < \Gamma_{d\sigma}^L + \Gamma_{d\sigma}^R$). This requires to go beyond the sequential tunneling description (see for instance [28]), i.e. to take also into account high-order quantum tunneling processes. For temperatures larger than the Kondo temperature of the circuit ($T > T_K$), this can be done by calculating the Green's functions $G_{d\sigma}(\omega)$ with the Equation of Motion Technique (E.O.M.) introduced for quantum dot systems by Meir *et al.* [31].

Single orbital case For simplicity, we first consider a one-orbital quantum dot. Then, the E.O.M technique leads to [31]

$$G_{d\sigma}(\omega) = \frac{\hbar(1 - \langle n_{d\bar{\sigma}} \rangle)}{\hbar\omega - \xi_{d\sigma} - \Sigma_{d\sigma}^0 + \frac{U\Sigma_{d\sigma}^1}{\hbar\omega - \xi_{d\sigma} - U - \Sigma_{d\sigma}^0 - \Sigma_{d\sigma}^3}} + \frac{\hbar \langle n_{d\bar{\sigma}} \rangle}{\hbar\omega - \xi_{d\sigma} - U - \Sigma_{d\sigma}^0 - \frac{U\Sigma_{d\sigma}^2}{\hbar\omega - \xi_{d\sigma} - \Sigma_{d\sigma}^0 - \Sigma_{d\sigma}^3}} \quad (9)$$

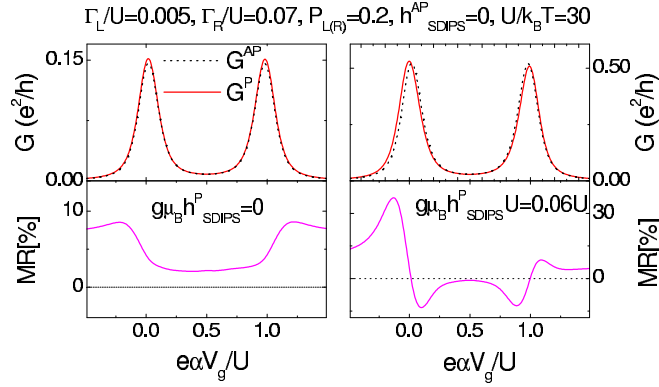


Figure 6. Top panels: Conductance G^P in the parallel configuration (red full lines) and conductance G^{AP} in the antiparallel configuration (black dotted lines) as a function of the gate voltage V_g , for the circuit shown in figure 2, with W a 1-orbital quantum dot. We have used $\Gamma_L = 0.005U$, $\Gamma_R = 0.07U$, $P_{L(R)} = 0.2$, $U/k_B T = 30$ and $h_{SDIPS}^{AP} = 0$. Bottom panels: Magnetoresistance MR (pink curves) corresponding to the above conductance plots. The results are shown for $g\mu_B h_{SDIPS}^P = 0$ (left panels) and $g\mu_B h_{SDIPS}^P = 0.06U$ (right panels).

where $\langle n_{d\sigma} \rangle = -\int_{-\infty}^{+\infty} d\omega f(\hbar\omega) \Im m[G_{d\sigma}^d(\omega)]/\pi$ is the average occupation of orbital d by electrons with spin σ . Assuming that the coupling to the leads is energy independent (broad band approximation), one has $\Sigma_{d\sigma}^0 = -i(\Gamma_{d\sigma}^L + \Gamma_{d\sigma}^R)/2$, $\Sigma_{d\bar{\sigma}}^3 = -i(\Gamma_{d\bar{\sigma}}^L + \Gamma_{d\bar{\sigma}}^R)$ and, for $i \in \{1, 2\}$,

$$\Sigma_{d\bar{\sigma}}^i = \sum_k \frac{\mu_i(\xi_{k\bar{\sigma}}) |t_{k\bar{\sigma}}^d|^2}{\hbar\omega - \xi_{d\sigma} + \xi_{d\bar{\sigma}} - \xi_{k\bar{\sigma}} + i0^+} + \sum_k \frac{\mu_i(\xi_{k\bar{\sigma}}) |t_{k\bar{\sigma}}^d|^2}{\hbar\omega - \xi_{d\sigma} - \xi_{d\bar{\sigma}} - nU + \xi_{k\bar{\sigma}} + i0^+}.$$

with $\mu_1(\xi) = f(\xi)$ and $\mu_2(\xi) = 1 - f(\xi)$. The term $\Sigma_{d\sigma}^0$, which is due to the tunneling of electrons with spin σ , already occurred in the non-interacting case. Indeed, for $U = 0$ and $T_l^\sigma \ll 1$, the conductance given by the above equations can be perfectly mapped onto the non-interacting conductance found in section 3.1, using $E_{d\sigma}^c = \xi_{d\sigma}$ and $T_l^\sigma = \pi N_{F\omega} \Gamma_{d\sigma}^l = 2\pi N_{F\omega} |\Sigma_{d\sigma}^0|$. In the interacting case, $G_{d\sigma}(\omega)$ also involves $\Sigma_{d\sigma, d'\sigma'}^{i,n}$ terms related to the tunneling of electrons with spin $\bar{\sigma}$. Note that $G_{d\sigma}$, $\xi_{d\sigma}$ and $\Gamma_{d\sigma}^{L(R)}$ depend on the configuration $c \in \{P, AP\}$ considered but for simplicity we have omitted the index c in those quantities.

Figure 6 shows the conductance G^c in configuration $c \in \{P, AP\}$ (top panels) and the magnetoresistance MR (bottom panels) calculated for different values of h_{SDIPS}^c , using $\Gamma_{d\sigma}^l = \Gamma_l(1 + \eta_l \sigma P_l)$ for $l \in \{L, R\}$. The conductance peak corresponding to level d is split by U due to Coulomb interactions. For $h_{SDIPS}^c = 0$ (left panels), we already note that although the two conductance peaks displayed by $G^P(V_g)$ are very similar, the MR variations corresponding to these two peaks have different shapes (see also [24]). More precisely, for the low values of polarization considered here, $MR(V_g)$ is approximately mirror symmetric from one conductance peak to the other. This is in contrast with the single channel non-interacting case in which the $MR(V_g)$ was identical for all conductance peaks. A finite effective field h_{SDIPS}^c produces a shift of

the conductance peaks from the P to the AP configurations. For instance, in figure 6, top right panel, the left [right] conductance peak is shifted to the right [left] from P to AP because it comes in majority from the transport of up [down] spins in the P case. As a consequence, in figure 6, bottom right panel, the amplitude of MR is enhanced and it becomes negative for certain values of V_g . We note that using a finite SDIPS does not help to obtain similar MR variations for the two peaks of $G^P(V_g)$ because the SDIPS shifts these two peaks in opposite directions.

Before concluding this section, we point out that, in principle, h_{SDIPS}^c is not the only term which can lead to a spin-splitting of the dot energy levels. Indeed, the terms proportional to $\Sigma_{d\bar{\sigma}}^1$ and $\Sigma_{d\bar{\sigma}}^2$ in equation (9) can also renormalize these levels, due to their real part. In the case of ferromagnetic contacts, this renormalization is different for the two spin directions. This allows to define another type of effective field, h_U^c , which is intrinsically taken into account in the treatment shown here. The effects of h_U^c have been studied in detail by [25] for a quantum dot with non-collinearly polarized ferromagnetic leads in the sequential tunneling regime (see note [34] of reference [16]), and by [27] for a quantum dot in the Kondo regime. Similarly to h_{SDIPS}^c , the value of h_U^c depends on the configuration of the ferromagnetic electrodes and it must vanish in the AP configuration for symmetric junctions. Nevertheless, for the low values of tunnel rates $\Gamma_{L(R)}$, polarizations $P_{L(R)}$ and the temperatures T used here, h_U^c is much weaker than the finite h_{SDIPS}^c assumed, and it can therefore not play the same role as h_{SDIPS}^c .

Generalization to a non-degenerate multilevel system For simplicity, we have considered in the previous section the one-orbital case. In practice, other orbital levels close to orbital d can modify the $MR(V_g)$ pattern. Nevertheless, for non degenerate energy levels with a sufficiently large intrinsic level spacing ΔE (see [16]), the two conductance peaks associated to a given orbital will occur consecutively in $G^c(V_g)$. The SDIPS will shift these two peaks in the same way as for the single orbital model. Therefore, one can still expect changes of sign in the $MR(V_g)$ curves, with dissimilar $MR(V_g)$ patterns for the two conductance peaks corresponding to a given orbital level.

Effect of a twofold degeneracy of orbital levels. In single wall carbon nanotubes, a two-fold orbital degeneracy is commonly observed, related to the K-K' energy band degeneracy of graphene [10, 11]. To investigate some consequences of this feature, one can consider a two degenerate orbitals model, i.e. hamiltonian (5) with $d \in \{K, K'\}$ and $\xi_{K'\sigma} = \xi_{K\sigma}$. For simplicity, we assume no coupling between the two orbitals through higher orders dot-lead tunnel processes. We also assume the same dot-lead coupling and interfacial parameters for both orbitals. In the non-interacting case, this modification leaves the MR unchanged (see section 3.1). In the interacting limit, an orbital degeneracy has more complicated effects on the MR . This was studied with the E.O.M. technique in reference [16]. We refer the readers to this reference for details of the calculation and present here the main results of this approach.

Figure 7 shows the conductance (top panels) and MR curves (bottom panels) in

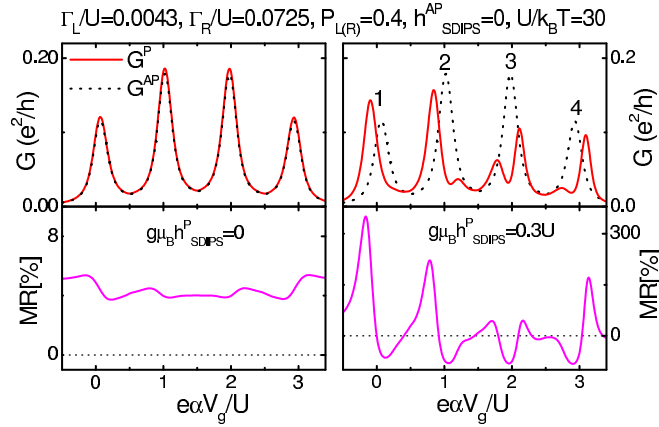


Figure 7. Top panels : Conductance G^P in the parallel configuration (red full lines) and conductance G^{AP} in the antiparallel configuration (black dotted lines), for the circuit of figure 2, with W a two-orbitals quantum dot. We have used identical tunnel rates to the two orbitals, i.e. $\Gamma_L = 0.0043U$, $\Gamma_R = 0.0725U$, and $P_{L(R)} = 0.4$. We have also used $U/k_B T = 30$ and $h_{SDIPS}^{AP} = 0$. Bottom panels: Magnetoresistance MR (pink full lines) corresponding to the conductance plots. The results are shown for $g\mu_B h_{SDIPS}^P = 0$ (left panels) and $g\mu_B h_{SDIPS}^P = 0.3U$ (right panels). The twofold orbital degeneracy allows to restore locally an approximate regularity of the $MR(V_g)$ pattern. This behavior will be compared with experimental results in section 5.2.3.

the two orbital case, calculated for different values of h_{SDIPS}^c . In most cases, the curves $G^c(V_g)$ show 4 resonances, the first two associated with a single occupation of K and K' , and the other two to double occupation. For $h_{SDIPS}^P = h_{SDIPS}^{AP} = 0$ and the parameters used here, the MR remains positive for any value of V_g (left panels). Like in the 1-orbital case, a finite h_{SDIPS}^c makes easier negative MR effects and allows a stronger tunability of the MR effect with V_g (right panels). Importantly, the effect of h_{SDIPS}^c again depends on the occupation of the dot and the $MR(V_g)$ pattern is thus not similar for the four conductance peaks. Nevertheless, in figure 7, top right panel, the first two conductance peaks of G^P (peaks 1 and 2) are both shifted to the left by h_{SDIPS}^P because they are both due in majority to up spins. This allows to get a MR pattern approximately similar for these two peaks, i.e. a transition from positive to negative values of MR (bottom right panel). On the contrary, peaks 3 and 4 correspond to a transition from negative to positive values of MR because the associated conductance peaks are due in majority to down spins. The shape of the $MR(V_g)$ pattern associated to the transition between peaks 3 and 4 is particular (negative/positive/negative) because, for the values of parameters considered here, Coulomb blockade does not entirely suppress the up spins contribution in peak 3. Remarkably, this allows to obtain, at the left of figure 7, bottom right panel, three positive MR maxima which differ in amplitude but have rather similar shapes. Taking into account a twofold orbital degeneracy thus allows to restore an approximate local regularity of the MR pattern. Note that for clarity, we have used in figure 7, right panels, a large value of h_{SDIPS}^P . Nevertheless, the effect persists for lower values of SDIPS (see figure 14). This behavior will be compared with

the experimental data of reference [29] in section 5.2.3.

3.3. Other interacting regimes.

In sections 3.1 and 3.2, we have put a special emphasis on the non-interacting regime and on the Coulomb blockade regime because this is relevant for interpreting the experimental results available so far (see section 5). However, in principle, a carbon nanotube connected to ferromagnetic leads can adopt other types of behaviors. For instance, it could behave as a quantum dot in the Kondo regime (see e.g. [32]). The effect of ferromagnetic leads on this system has been studied theoretically by various authors [26, 27]. A first experimental study could be realized using C_{60} molecules, revealing a spin-splitting of the Kondo resonance related to the coupling to the ferromagnetic leads [33]. Nevertheless, in carbon nanotubes, Kondo effect has only been observed with non-magnetic leads so far [34]. A carbon nanotube can also behave as a Luttinger liquid due to the interplay between electronic interactions and the one-dimensional nature of the nanotube [35, 36]. In a Luttinger liquid, electrons form collective charge and spin excitations which propagate with different velocities. The resulting spin-charge separation effect remains to be observed in an unambiguously accepted way [37]. This is one more fundamental motivation for the study of spin transport in carbon nanotubes. It has been predicted that spin-transport could provide experimental evidences of spin-charge separation, in the Fabry-Perot like regime [38] corresponding to section 3.1, as well as the incoherent regime $\max(eV_{sd}, k_B T) \gg \hbar v_{FW}/\ell$ (see [17]). We will not report on those predictions in detail here because no experimental realization is available at this time.

3.4. The spin injection problem.

Until now, we have assumed that it was possible to inject spins reliably in carbon nanotubes. More precisely, in the framework of the theories presented in sections 3.1 and 3.2, we have assumed that the spin polarization P_l^n of the tunnel rates was finite. One must wonder whether this is possible in practice.

In the last decade, the realization of spin-injection from ferromagnetic metals into semiconductors has triggered many efforts, motivated by the proposal by Datta and Das for a spin transistor based on the electric field control of spin-orbit coupling through the Rashba effect [2, 39]. One major difficulty came from the problem of the so-called conductivity mismatch. As shown by [40] in the diffusive limit, when a semiconductor is in good contact with a ferromagnetic material, the spin-polarization of the current injected into the semiconductor is strongly reduced because the conductivity of the semiconductor is much smaller than that of the ferromagnet. Nevertheless, it was shown that spin-injection can be enhanced by adding tunneling contacts at the interfaces between the ferromagnets and the non-magnetic materials [41, 42]. This turns out to be valid also in the ballistic limit (see for instance [43]), and in particular for carbon nanotubes, as illustrated in the next section.

3.4.1. The ballistic spin injection picture. Tunnel barriers are commonly obtained between ferromagnetic metals and carbon nanotubes. This makes spin injection possible as we are going to show here. Estimating accurately the spin injection parameter P_l^n for a ferromagnet/nanotube interface is beyond the scope of this review. We will rather adopt here a scattering approach with a Dirac potential barrier to model the interface. As shown by reference [43], this simplified approach is enough to capture some essential properties of the interfaces.

We assume a Dirac-function potential $U_l^\sigma \delta(x-x_l)$ for the interface $l \in \{L, R\}$ placed at x_l , and we use a spin-dependent wavevector k_l^σ for ferromagnetic lead l . Solving the quantum mechanical problem, one finds for junction l a transmission probability:

$$T_l^{n,\sigma} = \frac{4k_{Fw}k_l^\sigma}{(k_{Fw} + k_l^\sigma)^2 + (2U_l^\sigma m_e/\hbar^2)^2} \quad (10)$$

For completeness, we also give the expression of the wire-wire reflection phase

$$\varphi_l^{n,\sigma} = \arctan \left[\frac{2U_l^\sigma m_e}{\hbar^2(k_{Fw} - k_l^\sigma)} \right] + \arctan \left[\frac{2U_l^\sigma m_e}{\hbar^2(k_{Fw} + k_l^\sigma)} \right]$$

at contact l . Figure 8 shows the spin-averaged transmission probability $T_l^n = (T_l^{n,\uparrow} + T_l^{n,\downarrow})/2$, the spin-polarization of the transmission probability $P_l^n = (T_l^{n,\uparrow} - T_l^{n,\downarrow})/(T_l^{n,\uparrow} + T_l^{n,\downarrow})$ and the SDIPS parameter $\Delta\varphi_l^n = \varphi_l^{n,\uparrow} - \varphi_l^{n,\downarrow}$ calculated from these equations. For the nanotube, we use $k_{Fw} \sim 8.5 \cdot 10^9 m^{-1}$ [8], and for the ferromagnetic contact, we use the typical value $k_l^\sigma \sim 1.7 \cdot 10^{10} m^{-1}$ [43] and a spin polarization $p_l = 0.3$ for the electronic density of states in lead l . We define the average barrier strength $Z_l = m_e(U_l^\uparrow + U_l^\downarrow)/\hbar^2 k_{Fw}$. We first assume that U_l^σ is spin-independent (full curves). For a metallic contact, that is $Z_l = 0$, P_l^n remains very small. Nevertheless, the spin injection efficiency is strongly enhanced for a high barrier strength [43]. It is also possible that the potential barrier between the nanotube and the ferromagnet is itself spin-polarized, i.e. $\alpha_l = (U_l^\downarrow - U_l^\uparrow)/(U_l^\uparrow + U_l^\downarrow) \neq 0$. This can be due to the magnetic properties of the contact material itself, when it is evaporated directly on the nanotube, but it can also be obtained artificially by using a magnetic insulator (see [44]) to form the barrier. This allows to further enhance spin-injection (dashed lines).

Before concluding this section, we point out that in the case of coherent quantum transport, P_l^n is not the only parameter which sets the efficiency of spin-injection. Indeed, $\Delta\varphi_l^n$ is also a crucial parameter since it determines the localized quantum states inside the wire. Let us consider for simplicity the non-interacting case of section 3.1. For the weak values of SDIPS used in figure 4, spin injection was not improved. However, it was shown that with a stronger SDIPS, the resonant states in $G^{P[AP]}$ are spin-split, each sub-peak corresponding to a given spin-direction (see reference [18]). Having a strong SDIPS can thus allow to have a strongly spin-polarized current. Since the SDIPS-induced spin-splitting is different in the P and AP configurations, this allows to further increase the MR . One can see from figure 8 that the condition required for this effect can be obtained with weakly transparent and spin-dependent barriers (see dashed lines for Z_l large), which is compatible with having a large P_l^n .

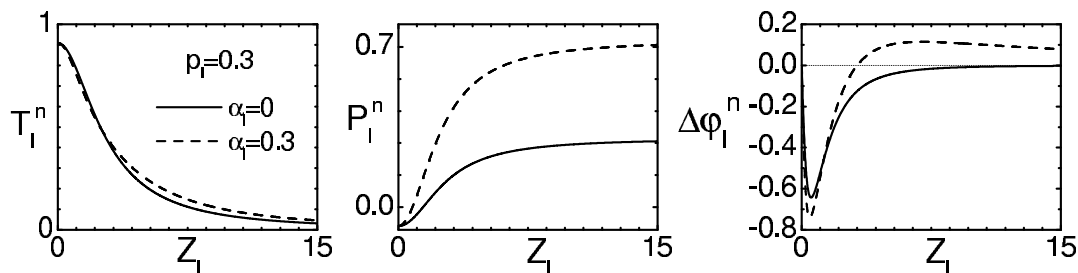


Figure 8. Spin-averaged tunneling rate T_l^n (left panel), tunneling rate polarization P_l^n (middle panel) and SDIPS parameter $\Delta\varphi_l^n$ (right panel) of contact $l \in \{L, R\}$, estimated by using a Dirac barrier model with a spin-dependent coefficient U_l^σ , placed between a ferromagnetic metal with Fermi wavevector $k_l^\sigma \sim 1.7 \cdot 10^{10} \text{m}^{-1}$, and a wire with Fermi wavevector $k_{Fw} = 8.5 \cdot 10^9 \text{m}^{-1}$ typical of single wall nanotubes. We show the results as a function of the average barrier strength $Z_l = m_e(U_l^\uparrow + U_l^\downarrow)/\hbar^2 k_{Fw}$, for a polarization $p_l = 0.3$ of the lead density of states and different values of the spin asymmetry $\alpha_l = (U_l^\downarrow - U_l^\uparrow)/(U_l^\uparrow + U_l^\downarrow)$ of the barrier.

3.4.2. Experimental identification of spin-injection In sections 3.1 and 3.2, we have considered the gate-tunable *MR*-effect produced by spin injection into the nanotube. We will introduce in section 4.2 other types of *MR* effects which are not due to spin-injection but to various properties of the ferromagnetic contacts. For proving that spin-injection is actually taking place in an experiment, one must be able to discriminate the spin-injection *MR* effect from contact *MR* effects.

For this purpose, one key idea is that the *MR* found in sections 3.1 and 3.2 is mainly a *two-terminal* effect. If only one of the contacts $k \in \{L, R\}$ is ferromagnetic, spin injection will still induce a hysteresis in G as a function of the external field H , but with only a very small change ΔG when $H = \pm H_{ck}$. This slight change will occur because the situations in which \vec{p}_k is parallel or antiparallel to \vec{H} are not totally equivalent according to equation (2). For instance, using the same parameters as in figure 4 but with $P_l = 0$ and $\Delta\varphi_l = 0$ for one of the two contacts ($l = L$ or $l = R$) and using the typical value $g\mu_B H_{ck} L/\hbar v_{FW} = 0.01$, one finds a value $|\Delta G|/G < 0.8\%$ much weaker than the maximum *MR* found for two ferromagnetic contacts in this figure. The situation seems to be different for contact *MR* effects: as we will see in section 4.2, these effects should already be significant with a single ferromagnetic contact if they are relevant with two ferromagnetic contacts. We will describe in section 4.2 other more specific features which can allow to identify contact *MR* effects.

4. Contacting carbon nanotubes with ferromagnetic contacts.

In this section, we present the state of the art in contacting carbon nanotubes with ferromagnetic materials. We emphasize the characteristics of the contacts such as minimum room temperature two probe resistance (or transmission) and the maximum *MR* amplitude. We also discuss contact effects which are not related to spin-dependent transport inside the nanotubes but which could sometimes be superimposed to the *MR*

effects described in the previous section.

4.1. Contacting carbon nanotubes with ferromagnetic leads.

Contacting carbon nanotubes with metallic electrodes has been an issue since the start of the study of their electronic properties. Most of transport measurements have been carried out in a two probe geometry. In the case of non-magnetic electrodes, the transmission of the contacts determines the relevant regime for charge transport. As we have seen above, connecting ferromagnetic contacts to carbon nanotubes raises additional questions, like e.g. the efficiency of spin injection. Therefore, the choice of the ferromagnet is not only crucial regarding the coupling of the electrodes to the nanotube but also regarding the reliability of spin injection.

In the case of non-magnetic contacts, few multi probe measurements have been carried out [45, 46] and provide new insights to quantum transport in nanotubes. Similarly, one can expect multi-probe measurements to provide useful information about spin transport when some of the probes are ferromagnetic [47, 48]. We will however focus on the studies of the two probe geometries since they are the most advanced carried out so far. Table 1 provides a summary of these works.

The main feature to be observed in a carbon nanotube connected to two ferromagnetic leads is a hysteresis of the resistance versus an applied magnetic field swept in two opposite directions, like shown in figure 1, right. One delicate point is the control of the switching of the magnetization. It turns out that it is non-trivial to control accurately the domain pattern of the ferromagnet nearby the contact with the nanotubes. Therefore, almost no MR curve look like the theoretical ones. The hysteresis curves often show complex structures. As we will see, this problem has been partially solved with $Ni_{1-x}Pd_x$ and $La_{2/3}Sr_{1/3}MnO_3$ ($LSMO$) contacts.

4.1.1. Co contacts. In the pioneering work by K. Tsukagoshi and co-workers, Co contacts were used to study spin-dependent transport in MWNTs [49]. The two-terminal resistance of the devices at room temperature was ranging from $8k\Omega$ to $250k\Omega$ [50]. At $4.2K$, the authors observed a MR which they attributed to spin transport along the relatively short MWNT length ($300nm$). The magnetic field was applied in-plane. The electrodes were both in Co and had the same geometry. Given that there was *a priori* no reason for having two different coercive field in the two electrodes, the AP configuration was difficult to identify. The amplitude of the hysteresis was at most of about +9%. The observed reduced value was attributed to spin relaxation in the nanotube, yielding a spin relaxation length of $l_s = 260nm$. The method was extended later to SWNTs devices [50]. Few experiments with multi-probes of Co were carried for SWNTs [47, 48]. In that case, the two-probe resistance was ranging from about $12k\Omega$ to $M\Omega$'s. The two-terminal MR reported was ranging from 2% to 6%. In reference [48], shape anisotropy was used to control selectively the switching of the different Co electrodes (typical width about 100nm). Experiments with Co electrodes were also carried out by Zhao and co-

Material	SWNT ($k\Omega$)	MWNT ($k\Omega$)	Max MR (%)	MR sign	Gate control	F-NT-N $\Delta G/G$ (%)	References
Co	15	8	36	+ and -	no	N	[47–51]
Fe	80	N	100	+ and -	yes	~ 0	[54, 55]
Ni	N	N	15	+ and -	yes	N	[56]
NiPd	11	5.6	17	+ and -	yes	< 1.4	[29, 57, 58]
(Ga,Mn)As	N	N	150	+ and -	yes	< 10	[54, 55]
LSMO	N	1000	37	+	no	N	[60]

Table 1. Summary of the various contacting materials used so far and their contacting properties. Columns 2 and 3 display the minimum two-probe resistance measured at room temperature for SWNTs and MWNTs contacted with the material indicated in column 1. Column 4 displays the maximum MR amplitude measured at low temperatures. Column 5 reports the MR signs observed. Column 6 indicates whether a gate control of the MR was achieved. Column 7 indicates the magnetic signal $\Delta G/G$ measured for nanotubes contacted with one ferromagnetic lead and one non-magnetic lead. Column 8 indicates the corresponding references (N=Not reported).

workers [51] but a negative MR of -36% was observed.

It is important to point out that the above experiments have been realized without a gate voltage supply V_g . In the absence of any doping, this would imply that the carbon nanotubes were operated at their charge-neutral point. However, it has been found that carbon nanotubes are extremely sensitive to their chemical environment. The chemical potential E_{F_w} of a nanotube can be strongly modified by surface adsorbates like water molecules, gas molecules or ions [22, 52, 53]. In sections 3.1 and 3.2, we have shown that the sign and amplitude of MR strongly depends on E_{F_w} . This implies that the spin signal will depend on details of the nanotube environment. One can even expect that MR differs significantly if one measures the same sample in different cool-downs, like observed in another experiment described in next section [54]. Therefore, although the different signs and amplitudes of MR found in the Co/nanotube experiments are compatible with the theoretical expectations, a further experimental investigation of the MR effect requires to use a gate electrode in order to study the dependence of MR with V_g , which is much more significant than the value of MR without a gate voltage supply.

4.1.2. Fe contacts. Fe is another possible choice for making ferromagnetic contacts on nanotubes. There is only one study using Fe on SWNTs carried out by A. Jensen and co-workers [54, 55]. In that case, the two terminal resistances reported at room temperature vary from $80k\Omega$ to $1M\Omega$. In this study, CVD grown SWNTs were used. The first contacts were made on the top of catalyst squares and had a typical size of $6\mu m \times 8\mu m$. The second contact design was two Fe electrodes with different aspect ratios, typically $10\mu m \times 300nm$ and $10\mu m \times 200nm$ in order to control the switching via shape anisotropy. However, both these contact geometries gave similar magnetization

switching for a field applied in plane. The samples were coupled to an electrostatic gate. The sign of the MR could be changed from positive to negative with the gate voltage. The observed MR was ranging from -50% up to 100% . Due to the absence of a detailed study of MR versus V_g , a clear conclusion cannot be drawn from this work.

Figure 9. Left : SEM micrograph of a typical F-nanotube-F sample of Sahoo *et al.* [29]. NiPd contacts are used to inject and detect spins electrically in a MWNT with a contact separation of about 400nm . The external magnetic field is applied in plane, either perpendicular or parallel to the axis of the elongated NiPd strips. Right : Statistics for the contacting scheme with NiPd on MWNTs. The typical two probe resistance at room temperature is $20k\Omega$.

4.1.3. Ni contacts. Ni has also been used to implement ferromagnetic electrodes on SWNTs [56]. The main findings with respect to the other works is a continuous sign change as a function of gate voltage, from $+10\%$ to -15% . Although the channel length was about 10nm , no size quantization was observed at 4.2K .

4.1.4. NiPd contacts. In principle, all kinds of ferromagnetic alloys could be tried in order to improve the reliability of the spin injection and/or the switching of the magnetization. Among these choices, Pd based alloys look particularly promising. Indeed, experiments using $Ni_{1-x}Pd_x$ with $x \sim 0.5$ are among the most advanced studies for spin transport in carbon nanotubes [29, 57, 58]. This choice is based on the observation that Pd alone makes reliable contacts on MWNTs as well as SWNTs [59]. Furthermore, Pd is close to the ferromagnetic instability with a Stoner enhancement of about 10. Few magnetic impurities are enough to drive it in the ferromagnetic state (the same holds for Pt which has a somewhat lower Stoner enhancement of about 4). Therefore, it seems possible to combine the good contacting properties of Pd with a finite spin polarization. Furthermore, the use of Pd as contacting metal prevents oxide layers from forming at the ferromagnet/nanotube interface. This might be an advantage with respect to the methods using pure ferromagnetic metals, because most of the ferromagnetic oxides are anti-ferromagnetic and therefore not only depolarize the electronic current, but also modify in general the spin activity of the interface.

S. Sahoo and co-workers [29, 58] were the first to study this contacting scheme on nanotubes. The type of devices studied is presented in figure 9. Two ferromagnetic $Pd_{0.3}Ni_{0.7}$ strips are used to contact either a MWNT or a SWNT. They have different shapes, typically $14 \mu\text{m} \times 0.1 \mu\text{m}$ and $3 \mu\text{m} \times 0.5 \mu\text{m}$ for the left and the right electrode respectively. The narrower electrode has a sharp switching around $100 - 250\text{mT}$. The wider one has a less pronounced switching, as shown on figure 10. This suggests that its magnetization gradually rotates upon reversing the sign of the external magnetic field. It is worth noting that H.T. Man et al. [57] as well as S. Sahoo et al. have found that the magnetic anisotropy of the NiPd strips is in plane, perpendicular to their long axis. This is in contradiction with the expected shape defined anisotropy and might be related the

complexity of the domain structure of the Pd based ferromagnetic alloys. The two probe resistance at room temperature of devices with MWNTs studied by Sahoo et al. [58] is summarized on the right panel of figure 9. As shown by this figure, the distribution of resistances is rather peaked at the typical value of $20k\Omega$, which shows the reliability of this contacting procedure. The minimum value is $5.6k\Omega$, the best ever reported for ferromagnetic contacts on MWNTs. For SWNTs, the transparency of the contacts is lower in general, but transmission probabilities as high as 0.84 have been reported by H.T. Man et al. [57].

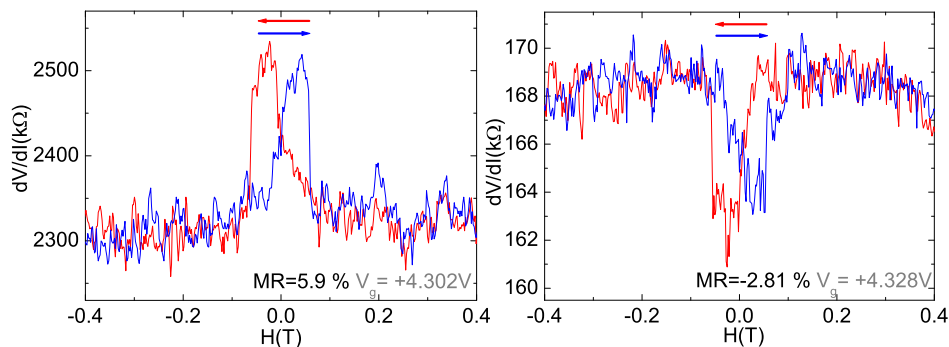


Figure 10. Example of magnetoresistance curves for the SWNT measurements of reference [29]. Depending on the gate voltage, both signs of the MR are observed. Left : the MR observed is positive ($MR = 5.89\%$), for a gate voltage $V_g = 4.302V$. Right : the MR observed for the same device is negative ($MR = -2.81\%$), for a gate voltage $V_g = 4.328V$.

At temperatures below $10K$, a MR is commonly observed upon sweeping an external magnetic field. Depending on the gate voltage, the MR is either positive or negative, as shown in figure 10. The amplitude of the effect is about 5% for MWNTs and SWNTs in the "Fabry-Perot" regime. It grows to about 10 – 15% for SWNTs in the Coulomb blockade regime. In addition, the sign of the MR can also be controlled by V_{sd} in both types of nanotubes [29, 57]

4.1.5. Other types of contacts. So far, we have only considered metallic ferromagnetic contacts to carbon nanotubes. This choice is generally led by the simplicity of the combination of thin metallic film growth with standard e-beam lithography techniques. The two main drawbacks of these methods are the small spin polarizations of the electrodes and the possible conductivity mismatch between the metal and the carbon nanotube.

The latter issue may be solved if the ferromagnetic contacts are ferromagnetic semiconductors. Such a method has been used recently by Jensen *et al.* who used

(Ga,Mn)As ferromagnetic electrode [54]. In this study, the Curie temperature of the contacts is about $70K$. Therefore, the contacts are ferromagnetic at temperatures relevant for quantum transport in carbon nanotubes, but they cannot be used for applications at room temperature. The maximum amplitude of the MR observed at $300mK$ is however very large, about 150%, and both signs of MR are observed. In addition, the sign and the amplitude of the MR depend on V_g and V_{sd} .

Hueso *et al.* [60] have used LSMO to electrically inject and detect spins in MWNTs. These materials have a bulk spin polarization of about 100%. A MR of 37% is observed at $5K$, and the spin signal persists up to 100K. Nevertheless, this scheme seems to produce samples with a high two-probe resistance of about $1M\Omega$ at 300K.

4.2. The effect of contacts not related to spin injection.

As we have seen in section 3, spin-polarized transport induces a MR effect for ferromagnetically contacted nanotubes. However, a spin valve-like behavior does not automatically imply that spin injection is actually taking place in the nanotube. This just means that the resistance depends on the relative directions of the magnetizations of the two ferromagnets. Although this can be enough for spintronic devices [61], from a fundamental point of view, it is essential to separate spin injection related phenomena from the others. In this section, we introduce MR effects not directly related to the existence of a spin-polarized transport inside the nanotube.

4.2.1. Stray field effects. Ferromagnetic electrodes not only induce a spin dependent scattering at their interface but also generate an external stray field which can be under certain circumstances of the order of a few $100mT$ [62]. Therefore, two ferromagnetic microstrips like shown in figure 9 can in principle generate a local magnetic field H_{loc} which will switch hysteretically as the magnetizations switch. Since low dimensional conductors are very often sensitive to external magnetic fields, it is possible for a MR to appear just because charges couple naturally to the vector potential (such a sensitivity is reflected in the conductance of nanotubes connected to non-magnetic leads). Importantly, if this mechanism is effective with two ferromagnetic contacts, it should also be significant if only one contact is ferromagnetic, in contrast to the spin injection case.

In practice, a MWNT with ferromagnetic contacts has indeed in general a finite background MR superimposed to the hysteretic part of the MR . The field dependence of the non-hysteretic part of MR can be quantified by a sensitivity S in $\%/T$ to the local magnetic field. Figure 11 shows typical examples of hysteretic and background MR for a MWNTs with NiPd contacts, for different applied gate voltages V_g [29]. The sensitivity S is of the order of $1\%/T$ or less and can change sign for different V_g . From this figure, one can calculate the local field change ΔH_{loc} required to obtain the observed hysteretic MR . For $V_g = -3.1V$, one finds $\Delta H_{loc} = -2.9/0.2 = -14.5T$, which is negative and way beyond what can be obtained with microstrips. Furthermore, for $V_g = -3.3V$,

one would need a positive ΔH_{loc} , since both MR and S have the same negative sign. Such a sign change of the local magnetic field produced by two metallic ferromagnets for different gate voltages can hardly be explained. Therefore, stray field effects are not dominant in the MR signal for this type of F-MWNT-F device. In addition, as one can see in figure 10, S is in general smaller for SWNTs [29, 56, 57]. One can conclude that stray field effects do not contribute substantially to the MR observed in nanotubes, at least for the NiPd devices realized so far.

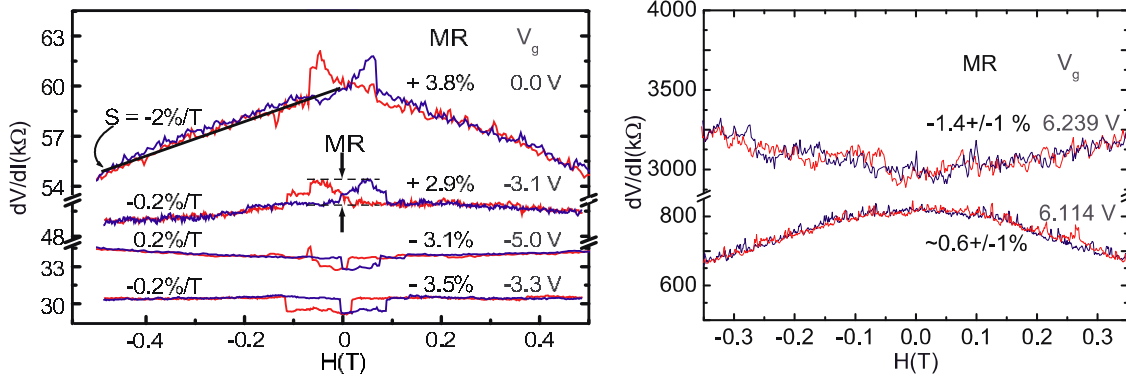


Figure 11. Left : MR observed by Sahoo *et al.* [29] for a MWNT connected to two NiPd leads, with different values of V_g . Depending on V_g , both signs of MR and sensitivity S are observed. The amplitude and the sign of S are not correlated with the MR . Therefore, the potential stray fields from the ferromagnetic electrodes cannot account for the MR observed for this device. Right : Resistance of a Pd-SWNT-PdNi device as a function of an external magnetic field for two values of V_g . Almost no hysteresis is observed. The maximum amplitude that can be estimated (almost within the noise) as $\Delta G/G \sim 1\%$, more than an order of magnitude smaller than the observed signal with two NiPd electrodes.

4.2.2. Magneto-Coulomb (MC) effects. The magnetic field used to control the magnetization of the ferromagnetic contacts can also induce a magnetoresistance effect, independently of any spin-polarized transport process. This so-called magneto-Coulomb (MC) effect [63] simply requires that the conductance of the nanotube depends on its gate voltage V_g . The magnetic field shifts the energies of spins \uparrow (\downarrow) inside contact l by the Zeeman energy $\pm g\mu_B H/2$. Since the densities of states $N_{l,\sigma} = N_l(1 + \sigma\eta_l p_l)$ in contacts $l \in \{L, R\}$ are spin dependent ($p_l \neq 0$), this Zeeman shift must be compensated by a slight change $\Delta\mu_l = -p_l g\mu_B H/2$ in the Fermi energies of the contacts. This modifies the electrostatic profile of the circuit, leading to a conductance $\tilde{G}(V_g) = G(V_g - C_L\Delta\mu_L/e - C_R\Delta\mu_R/e)$. In this framework, a hysteretic conductance pattern can be obtained while sweeping the magnetic field to reverse the magnetization of the contacts. The amplitude of the magnetoresistance signal induced by the MC effect is [64]

$$MR = -\frac{1}{G} \frac{dG}{dV_g} \frac{g\mu_B (p_L C_L H_{cL} + p_R C_R H_{cR})}{eC_g} \quad (11)$$

The expression of G to insert in (11) depends on the different energy scales involved in the problem. For a device showing conductance peaks, the MC effect should induce a magnetoresistance effect with a sign oscillating with V_g , since it is proportional to the derivative of $G(V_g)$. Importantly, equation (11) shows that the MC-induced magnetoresistance effect should occur even in the presence of one single ferromagnetic contact. At last, from the expression of $\tilde{G}(V_g)$, the MC effect produces a strong background variation in $G(H)$ on top of the discontinuities at $H = H_{cL(R)}$ (see [64]). These features could be useful for an experimental identification of this effect.

4.2.3. Comparison between single and double ferromagnetic contacts schemes. Both the stray field effect mechanism as well as the MC effect should already be significant for devices with a single ferromagnetic contact if these effects are relevant with two ferromagnetic contacts. Therefore, it is useful to fabricate such devices and measure the $\Delta G/G$. Such experiments have been carried out by Jensen *et al.* with Fe-NT-Au contacts and no MR has ever been found [55]. With (Ga,Mn)As contacts, Jensen *et al.* have reported a finite MR of about 10% for single ferromagnetic contacts, while the maximum amplitude for double ferromagnetic contacts is about 150%. Figure 11, right shows the $\Delta G/G$ measurement performed by [29] for a NiPd-SWNT-Pd device, for two different values of gate voltages, one in the Coulomb valley, and the other close to a resonance. The upper bound for $\Delta G/G$ is 1.4% in amplitude which is one order of magnitude lower than the maximum $\Delta G/G$ observed with two ferromagnetic contacts, as can be seen in figure 14. Therefore, all the studies carried out so far point to the fact that contact effect are generally not dominant.

5. Electric field control of spin transport.

In this section, we present the most advanced experimental results which have been reported so far about the electric field control of spin-dependent transport in carbon nanotubes. All these experiments have been realized with NiPd contacts. For their interpretation, we focus on the Fabry-Perot and quantum dot regimes, which have been introduced theoretically in section 3.

5.1. Spectroscopy of carbon nanotubes with ferromagnetic contacts.

The spectroscopy of a carbon nanotube contacted to ferromagnetic leads can be realized by measuring its conductance as a function of the gate voltage V_g and the source-drain voltage V_{sd} . This step is essential to determine the different characteristic energies which set the behavior of the nanotube and understand the physics leading to the MR effect. In the Fabry-Perot regime, the spectroscopy reveals the intrinsic energy spacing $\Delta E = \hbar v_{Fw}/2\ell$ of the quasi bound-states of the nanotube, where ℓ is the effective nanotube length on which transport is actually taking place (see figure 12, left panel). This length is generally defined by the inner spacing between the two metallic electrodes

for SWNTs (see for instance [10]) but can also be related to the full tube length for MWNTs [65]. In case of a quantum dot behavior, the spectroscopy also reveals the charging energy $U = e^2/C_\Sigma$ of the nanotube device (see figure 14, left panel). In the latter case, other energy scales can be revealed in the fine structure of spectroscopy in metallic SWNTs [10], but we will omit them since they have not been identified in the F-SWNT-F experiments so far.

5.2. Gate modulations of the magnetoresistance

We have shown in section 3 that the MR of a quantum wire with ferromagnetic contacts can strongly depend on the gate voltage V_g , in the Fabry-Perot regime as well as in the quantum dot regime. We show below how these phenomena can be revealed in ferromagnetically contacted MWNTs and SWNTs.

5.2.1. SWNTs in the Fabry-Perot regime Man *et al.* [57] have measured the MR for SWNTs with transparent NiPd contacts. In agreement with previous studies with non-ferromagnetic contacts, the characteristic pattern of an electronic interferometer is observed, as shown on figure 12 left panel. The pattern reveals an intrinsic level spacing $\Delta E \sim 7meV$, which corresponds to zero-dimensional states delocalized over $300nm$, in agreement with the lithographically defined SWNT length. Figure 12, right panel displays simultaneous measurements of the MR and the linear conductance G^P . The MR oscillates from 0% to 4% on the same gate scale as the linear conductance, e.g. $\Delta V_g \approx 0.5V$. Therefore, as anticipated from section 3.1, the MR can be gate controlled in SWNTs through quantum interferences.

Figure 12. Experimental results obtained by reference [57] with a SWNT connected to two PdNi contacts. The left panel shows a colorscale plot of the non-linear conductance G^P of the nanotube as a function of the source-drain voltage V_{sd} and the gate voltage V_g . The spacing between the resonant lines of conductance indicate an intrinsic energy spacing of the levels by $\Delta E \approx 7meV$. The right panel shows a comparison between the $G^P(V_g)$ and $MR(V_g)$ data measured at $T = 4.2K$ (symbols) and the non-interacting scattering theory of section 3.1.2, assuming two uncoupled channels with $T_L = 0.84$, $T_R = 0.26$, $P_{L(R)} = 0.1$ and no SDIPS.

In order to rule out possible contact effects, one can compare the experimental MR measured by [57] with the MR expected from the magneto-Coulomb effect. In principle, the so-called magneto-Coulomb (MC) effect can occur even in a non-interacting resonant wire since the conductance of the wire depends on its gate voltage V_g . The amplitude expected for the MC-induced magnetoresistance, using equation (11) with $C_g/C_\Sigma = 0.014$, $G(dG/dV_g)^{-1} = 0.125V$, $H_{cL(R)} < 300$ mT, $p_{L(R)} = 0.1$, is $|MR| < 0.2\%$. This value is much weaker than the measured MR . Also, the experimental $MR(V_g)$ signal is clearly not proportional to the logarithmic derivative of $G(V_g)$, in contrast to the MR expected from equation (11). It is thus not possible

to attribute the $MR(V_g)$ observed to the magneto-coulomb effect introduced in section 4.2.2.

Figure 13. Experimental results obtained by reference [29] with a MWNT connected to two PdNi contacts. Panel (a) shows the MR data measured at $T = 1.85$ K. The MR oscillates with a period $\Delta V_g^{TMR} \sim 0.4 - 0.75$ V. Panel (b) shows a colorscale plot of the non-linear conductance G^P of the nanotube as a function of the source-drain voltage V_{sd} and the gate voltage V_g , for $T = 300$ mK. This plot allows to resolve the single electron states, which correspond to a gate voltage scale $\Delta V_g^e \sim 25$ mV, and indicates Coulomb blockade effects. Panel (c) shows the conductance G^P of the device measured at $T = 300$ mK on a V_g range much larger than Panel (b). The conductance peaks show beatings with a period $\Delta V_g^{beat} \sim 0.4$ V comparable to ΔV_g^{TMR} .

Resonant effects account much better for the observed MR . Indeed, Man *et al.* [57] have interpreted their data with the model presented in section 3.1 [equations (1) and (2)]. They have assumed two uncoupled identical channels in order to take into account the two-fold degeneracy commonly observed in SWNTs, with $T_L = 0.84$, $T_R = 0.26$, $P_L = P_R = 0.1$ and no SDIPS. In view of the strong value of $T_L + T_R$ and of the low values of $P_{L(R)}$, the effects of the SDIPS on the $MR(V_g)$ curves are indeed probably too weak to be resolved in the actual experiment. Nevertheless, it is interesting to note that the $MR(V_g)$ pattern of figure 12, right panel, shows a slightly asymmetric behavior for $V_g < 7.7$ V, similarly to the curve shown in the bottom right panel of figure 4, plotted for $T_L = 0.84$, $T_R = 0.26$, $P_L = P_R = 0.1$ and a finite SDIPS value $\Delta\varphi_{L(R)} = -0.035$. The irregularities present in the variations of the $MR(V_g)$ data for $V_g > 7.7$ V prevent from concluding reliably on the presence of SDIPS in these data (the authors suggest that these irregularities are due to the the misorientation of the magnetizations in the electrodes).

5.2.2. MWNTs. Sahoo *et al.* [29] have studied the gate dependence of the MR for MWNTs with NiPd electrodes, at $T = 1.85$ K. As shown in figure 13a, the MR is observed to oscillate relatively regularly between -5% and $+6\%$ on a gate-voltage scale ΔV_g^{TMR} such that $0.4V < \Delta V_g^{TMR} < 0.75V$.

The conductance of the same sample has been studied at lower temperatures ($T = 300$ mK), in order to resolve the single-electron states which could not be resolved at the temperature at which the MR was measured. A measurement of the differential conductance dI/dV as a function of source-drain V_{sd} and gate voltage V_g at $T = 300$ mK is shown in figure 13-b for a relatively narrow V_g range. It displays the diamond-like pattern characteristic for single-electron tunnelling in a quantum dot. The diamonds vary in size with single electron addition energies ranging between 0.5 and 0.75 meV, in agreement with previous reports on MWNT quantum dots with non-ferromagnetic leads [65]. The MR gate-voltage scale ΔV_g^{TMR} measured at $T = 1.85$ K is much larger than the scale $\Delta V_g^e \sim 25$ mV for the addition of single electrons: it corresponds to the addition of at least 16 electrons rather than 1.

In order to understand this discrepancy, one can consider the linear conductance observed over a wider gate-voltage range, as shown in figure 13-c. The single-electron conductance peaks are strongly modulated in amplitude, leading to a regular beating pattern with a gate-voltage scale $\Delta V_g^{beat} \sim 0.4$ V. This scale corresponds to the scale ΔV_g^{TMR} of the MR oscillations, probably because, due to thermal averaging at $T = 1.85$ K, the conductance is determined by the envelope of these beatings, which affects in turn the magnetoresistance.

Interestingly, such beatings can be found within the multi-channel non-interacting picture introduced in section 3.1.3. In this model, at temperatures such that the single-particle resonances are averaged out, the MR is only sensitive to the average over these resonances, yielding a MR modulation that follows the envelope function of the single-electron peaks (see figure 5).

5.2.3. SWNTs in the Coulomb blockade regime Sahoo et al. [29] have also studied the MR for SWNTs with NiPd contacts. Figure 14 left panel displays the color plot of the non-linear conductance dI/dV as a function of V_g and V_{sd} at 1.85K for a SWNT device with NiPd electrodes. The characteristic quantum dot behavior is observed. One has $Ec \sim 5meV$ and $\Delta E \sim 2.5meV$. The latter value corresponds to zero-dimensional states delocalized on $\ell = 600nm$, in agreement with the lithographically defined SWNT length. In figure 14 right panel, the variations of the linear conductance G and the MR are simultaneously shown for two resonances. The MR changes sign on each conductance resonance. The amplitude of the MR ranges from -7% to $+17\%$, which is a higher amplitude than for the MWNT samples and SWNTs in the strongly coupled regime. Electron-electron interactions seem to enhance the amplitude of MR modulations, thereby improving the spin-FET behavior.

In this paragraph, we compare the experimental MR reported in [29] with the MR expected from the magneto-Coulomb effect. One can evaluate the amplitude of the magnetoresistance induced by the MC effect in this experiment, using equation (11). With $C_\Sigma/C_g = 10$, $G(dG/dV_g)^{-1} = 12.5mV$, $H_{cL(R)} < 100$ mT, $p_{L(R)} = 0.4$, one obtains an amplitude $|MR| < 0.4\%$, which is too weak to account for the data of figure 14. Also, the shape of the $MR(V_g)$ shown in this figure is clearly not proportional to the logarithmic derivative of $G(V_g)$, contrarily to what is expected for the MC-induced magnetoresistance. At last, circuits with a single ferromagnetic contact were also realized in order to check the origin of the MR effect observed. With a single ferromagnetic contact, the MR -effect obtained (see figure 11) is much weaker, which rules out the MC effect but also stray field effects produced by the ferromagnetic leads. Therefore, one can consider the MR observed with two ferromagnetic contacts as an effect of spin-injection in a resonant system.

In reference [29], Sahoo et al. have used the scattering approach introduced in section 3.1 in order to interpret their data. The line shape of the MR dips is asymmetric, similarly to the calculated line shape for the non-interacting regime displayed in figure 4 left panel. This suggests that a finite SDIPS can be observed in this circuit.

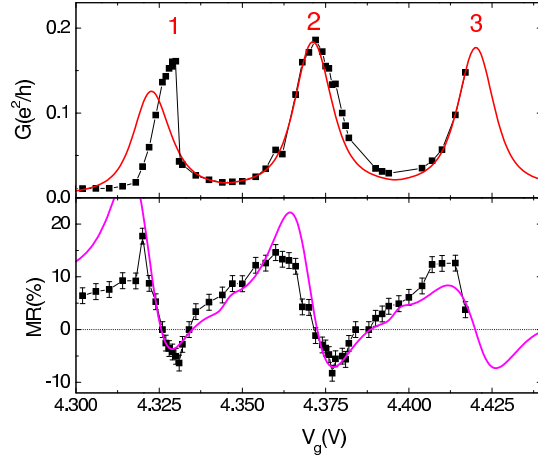


Figure 14. Experimental results obtained by reference [29] with a SWNT connected to two PdNi contacts. Left panel: colorscale plot of the non-linear conductance G^P of the nanotube as a function of the source-drain voltage V_{sd} and the gate voltage V_g . This plot indicates an intrinsic energy spacing of the levels by $\Delta E = 2.5\text{meV}$ and a charging energy $U = 5\text{meV}$. Right panel: conductance G^P and magnetoresistance MR measured simultaneously at $T = 1.85\text{K}$ (black squares). As shown by reference [16], these curves can be interpreted in an interacting picture by using the E.O.M approach presented in section 3.2 for a quantum dot with two degenerate energy levels. The theoretical curves are shown for parameters consistent with the experiment, i.e. $U = 5\text{ meV}$, $U/k_B T = 30$, $\alpha = 0.0986$ and $P_{L(R)} = 0.4$. Assuming identical tunnel couplings for the two orbitals, the values of tunnels rates $\Gamma_L = 0.0043U$ and $\Gamma_R = 0.0725U$ are imposed by the width and height of the conductance peaks. Then, $h_{SDIPS}^{P[AP]}$ are the only truly free fitting parameters remaining for interpreting the MR curve. The theory (colored full lines) is plotted here for $g\mu_B h_{SDIPS}^P = 0.05U$ and $h_{SDIPS}^{AP} = 0$.

Nevertheless, an interacting approach which takes into account Coulomb blockade is required in order to confirm this point. We discuss below a fully interacting approach which allows to fit quantitatively the data, as shown in figure 14, right panel.

Reference [16] has provided an interacting interpretation of the data, using the E.O.M. approach presented in section 3.2. The regularity of the $MR(V_g)$ oscillations displayed by the data being incompatible with a 1-orbital model, a two-degenerate-orbital model, which takes into account the K-K' degeneracy the orbital levels of the nanotube, has to be used. The two-orbital model exhibits a good agreement with the experimental data for $h_{SDIPS}^P = 0.05U$, $h_{SDIPS}^{AP} = 0$, $\Gamma_L/U = 0.0043$, $\Gamma_R/U = 0.0725$, $|P_{L(R)}| = 0.4$, $U = 5\text{ meV}$, $U/k_B T = 30$, and $\alpha = 0.0986$. Note that the two-orbital model could not provide a reasonable fit to the data for $h_{SDIPS}^{P[AP]} = 0$.

The value of h_{SDIPS}^P for the best fit corresponds to a magnetic field of about 2 T, which is too strong to be attributed to stray fields from the ferromagnetic electrodes (see section 4.2.1). For comparison, one can estimate h_{SDIPS}^P in the non-interacting theory [18], using realistic parameters i.e leads with a Fermi energy 10 eV and a density of states polarized by 40%, and a nanotube with Fermi wavevector $8.5 \cdot 10^9\text{m}^{-1}$,

Fermi velocity [8] $v_{Fw} = 8 \cdot 10^5 \text{ m.s}^{-1}$, length $\ell = 500 \text{ nm}$ like in reference [29], and density of states $N_{Fw} = 2\ell/\pi\hbar v_{Fw}$. The interfaces between the nanotube and the leads are furthermore modeled with Dirac potential barriers, with a height which is spin-polarized by 40% and an average value which corresponds to (see section 3.2) $\Gamma_{L(R)} = T_{L(R)}/2\pi N_F^{L(R)} \sim 60 \mu\text{eV}$ (For comparison the fitting parameters used in Fig. 14 correspond to $\Gamma_L = 21 \mu\text{eV}$ and $\Gamma_R = 362 \mu\text{eV}$). This gives $h_{SDIPS}^P \sim 1.3 \text{ T}$, which is consistent with the above value used for the fit.

Note that the fitting curves shown in figure 14 have been optimized in order to interpret the data for $V_g > 4.331 \text{ V}$. Like many Coulomb blockade devices, the nanotube circuit studied in this experiment suffered from low frequency V_g -noise, which can be attributed to charge fluctuators located in the vicinity of the device. At $V_g = 4.331 \text{ V}$, a gate voltage jump occurred. Therefore, one cannot be sure that the data for $V_g > 4.331 \text{ V}$ and $V_g < 4.331 \text{ V}$ correspond to the filling of consecutive levels. Nevertheless, there is a certain probability that this is the case since these gate voltage jumps have often an amplitude which does not exceed e/C_g . In this case, the discrepancy between the theory and the data could be due to the presence of other levels which should modify the theory for peak 1. In future experiments, it would be interesting to obtain continuous data on a larger V_g -range, in order to check that the shape of the $MR(V_g)$ pattern depends on the occupation of the dot (a different shape is expected for peak 4 in the theory of Ref. [16]).

5.3. Effect of source-drain bias on the magnetoresistance

The effect of source-drain bias V_{sd} on the MR can also be investigated in order to obtain a further understanding of the system. The MR at finite bias can be defined as $(dV/dI_{AP} - dV/dI_P)/(dV/dI_P)$.

Figure 15 displays two examples of MR as a function of V_{sd} . The left panel shows a measurement by S. Sahoo [66] of a MWNT with NiPd contacts separated by $1\mu\text{m}$ (this is a different MWNT sample than the one discussed in section 5.2.2). The MR , which is about 3% at zero bias, gradually decreases at finite bias and vanishes for $V_{sd} > 3\text{mV}$. It displays a sign change, symmetrically for $|V_{sd}| = 1\text{mV}$. This energy scale corresponds to the Zero Bias Anomaly (ZBA) observed in the conductance data shown above the MR . This ZBA has been reported in MWNTs and SWNTs. In the latter case, it has been attributed to Luttinger Liquid behavior [36]. In MWNTs, the ZBA has been attributed to the interplay of electron-electron interactions and disorder [68]. Figure 15, right panel, shows the gate voltage averaged MR of a SWNT measured by Man *et al.* [57] (this is the sample introduced in section 5.2.1). A similar trend as for MWNTs is observed.

Within the non-interacting picture, the MR should display a similar dependence versus finite bias as versus gate voltage. However, the general features found experimentally contradict this simple assumption. The discrepancy between the non-interacting model and the data of figure 15 might therefore be due to interactions. In the interacting case, Coulomb blockade can induce a non-trivial dependence of MR

versus V_{sd} [23]. For instance, Dynamical Spin Blockade is expected to strongly affect spin transport at finite bias in quantum dots in the sequential tunneling regime [28]. Non trivial variations of $MR(V_{sd})$ are also expected in the cotunneling regime [24]. Furthermore, oscillations of the MR signal are predicted in the Luttinger Liquid limit [17]. However, the fact that the MR does not seem to saturate to its classical value (i.e. that for two tunnel junctions in series) but rather vanishes at high bias points to possible spin relaxation processes in the nanotube or to a bias dependence of the spin polarization in the electrodes [57].

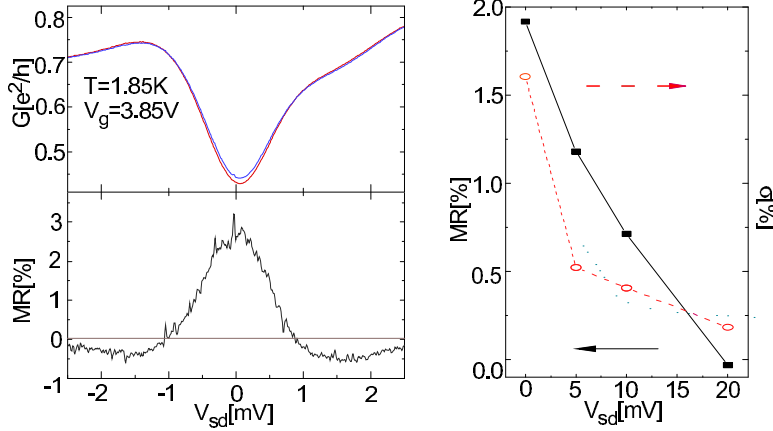


Figure 15. Effect of a finite source-drain voltage V_{sd} on the magnetoresistance of a carbon nanotube. The left panel corresponds to a MWNT study by Sahoo *et al.* [66]. The MR is displayed below the corresponding conductances in the AP (red full line) and the P orientations (blue full line), for a finite gate voltage of $3.85V$. The right panel corresponds to the SWNT study of Man *et al.* [57]. MR corresponds here to a gate voltage averaged MR and σ is the corresponding standard deviation. In both cases, the MR signal vanishes when the source drain voltage increases.

5.4. Spin relaxation time

We have reported above on various experiments which indicate that a carbon nanotube can convey a spin-polarized current. The success of these experiments relies on the fact that electrons have a sufficiently long spin relaxation time τ_s inside the nanotube. Nevertheless, for realizing a further control of the spin dynamics in nanotubes, a detailed study of spin relaxation processes would be useful.

On the theoretical side, few predictions for the value of τ_s in carbon nanotubes are available [72]. In thin films made out of usual metals like Cu, one finds $\tau_s \sim 10ps$ at low temperatures [70] due to mechanisms involving spin-orbit coupling and momentum scattering [39]. In principle, one can expect a much larger τ_s in nanotubes, due to the very weak spin-orbit interaction expected [21, 73] and the possible ballistic transport in these systems. Electronic confinement should further suppress conventional spin relaxation processes, as shown by [71] for GaAs quantum dots. One can thus expect that the dominant intrinsic relaxation mechanism arises from hyperfine coupling to the

nuclear spins [39]. Nevertheless, the latter mechanism may not be so critical since ^{12}C does not have a nuclear spin and ^{13}C , which has a nuclear spin $I = 1/2$, has a low natural abundance of 1.1%. Very recently, Semenov *et al.* estimated $\tau_s \sim 1\text{s}$ due to the hyperfine interaction, for semiconducting SWNTs at $T = 4\text{K}$ [72].

On the experimental side, two different types of methods can be used to measure τ_s in nanotubes : spin injection methods and spectral methods. Regarding spin-injection, spin must be conserved for at least the dwell time of the electron on the nanotube in order to produce a finite spin signal in the conductance of the whole device. This allows to estimate a lower bound for τ_s from the experiments reported in this review. From the measurements on SWNTs with NiPd contact in the weakly coupled regime [29], one finds $\tau_s > 2\hbar/(\Gamma_L + \Gamma_R) \sim 3\text{ps}$ at $T = 1.85\text{K}$. Regarding spectral methods, Conduction Electron Spin Resonance (CESR) has been used to investigate the spin relaxation processes in macroscopic amounts of carbon nanotubes [74, 75]. So far, no consensus has emerged from these measurements, especially concerning chemically undoped SWNTs. However, in all these experiments, it is found that magnetic impurities (probably catalytic particles) dominate the signal in general for unpurified nanotubes. For vacuum-annealed SWNTs, Petit *et al.* could restore a finite CESR signal and determine a relatively long τ_s of $3 - 5\text{ns}$ at $T = 300\text{K}$. Nevertheless this result has not been reproduced in later experiments [75]. Further research on spin relaxation mechanisms in nanotubes is highly desirable.

6. Conclusion and perspectives

In this review, we have shown that carbon nanotubes are promising candidates for the realization of efficient spin-transistors. Ferromagnetic contacts can be used to inject a spin polarized current inside the nanotube, allowing to observe a spin-valve behavior. A gate-tunability of the nanotube magnetoresistance has been observed, in agreement with theoretical predictions made for resonant tunneling systems and quantum dots.

From a technical point of view, the presently most advanced experiments regarding the gate-control of the magnetoresistance are not those which show the most efficient spin-injection. An optimization of the contact properties has still to be done in this kind of experiment, in order to obtain an accurate gate control of the giant magnetoresistance effect. Experiments with highly polarized ferromagnetic materials should be further developed in order to increase the efficiency of spin injection and thus the amplitude of the *MR* effect. Another possibility to investigate is using ferromagnetic insulators as tunnel barriers. The shape of the ferromagnetic contacts should also be optimized in order to get a better control of the switching behavior of the magnetic polarizations. Another problem is the low temperatures required in order to obtain discrete levels on the nanotubes. In order to increase the operating temperature of the carbon nanotube based spinFET, one could reduce the spacing between the ferromagnetic electrodes down to few 10nm, as suggested very recently [76].

From a fundamental point of view, a more extensive study of the dependence

of the nanotube magnetoresistance on the gate voltage, the source drain voltage and the temperature would allow to refine the understanding of the physics involved. For instance, it would be interesting to investigate the effects of the gate voltage on the contacts scattering properties. It would also be interesting to study how the Spin-Dependence of Interfacial Phase Shifts varies with the polarization of the contacts. Nanotube spin-valves could also be used in non-collinear configurations in order to study spin-precession effects. Eventually, the relevant spin relaxation mechanisms should be identified.

The studies introduced in this review open a path to the control and the manipulation of spin in nanotubes. Besides to spintronics applications, we believe that devices such as the ones depicted here could also prove to be useful for quantum computing applications.

Acknowledgments

A.C. and T.K. acknowledge fruitful discussions with G. Bauer, R. Egger, A. Fert, H. Jaffrès, P. Señor C. Strunk and H.S.J van der Zant. H.T.M. and A.F.M. gratefully acknowledge FOM and NWO (Vernieuwingsimpuls 2000 program) for financial support. M.-S.C. is supported by the SRC/ERC program (R11-2000-071) and the KFR Grant (KRF-2005-070-C00055). This work was financially supported by the RTN Spintronics, DIENOW, by the Swiss NSF and the NCCR Nanoscience. A.C. is financially supported by Région Ile-de-France.

References

- [1] G.A. Prinz, *Science* **282**, 1660 (1998).
- [2] S. Datta and B. Das, *Appl. Phys. Lett.* **56**, 665 (1990).
- [3] Th. Schäpers, J. Nitta, H. B. Heersche, and H. Takayanagi, *Phys. Rev. B* **64**, 125314 (2001).
- [4] M. N. Baibich, J. M. Broto, A. Fert, F. Nguyen van Dau and F. Petroff, *Phys. Rev. Lett.* **61**, 2472 (1988).
- [5] G. Binasch, P. Grünberg, F. Saurenbach and W. Zinn, *Phys. Rev. B* **39**, 4828 (1989).
- [6] M. Julliere, *Phys. Lett. A* **54**, 225 (1975).
- [7] S. J. Tans, M.H. Devoret, J. A. Groeneveld and C. Dekker, *Nature* **394**, 761 (1998).
- [8] W. Liang, M. Bockrath, D. Bozovic, J.H. Hafner, M. Tinkham and H. Park, *Nature* **411**, 665 (2001).
- [9] Ya. M. Blanter and M. Büttiker, *Phys. Rep.* **336**, 1 (2000).
- [10] S. Sapmaz, P. Jarillo-Herrero, J. Kong, C. Dekker, L. P. Kouwenhoven, and H. S. J. van der Zant, *Phys. Rev. B* **71**, 153402 (2005).
- [11] W. Liang, M. Bockrath, and H. Park, *Phys. Rev. Lett.* **88**, 126801 (2002); B. Babic and C. Schönenberger, *Phys. Rev. B* **70**, 195408 (2004); P. Jarillo-Herrero, J. Kong, H. S. J. van der Zant, C. Dekker, L. P. Kouwenhoven, and S. De Franceschi, *Phys. Rev. Lett.* **94**, 156802 (2005); S. Moriyama, T. Fuse, M. Suzuki, Y. Aoyagi, and K. Ishibashi, *Phys. Rev. Lett.* **94**, 186806 (2005).
- [12] E. Y. Tsymlal, A. Sokolov, I. F. Sabirianov, and B. Doudin, *Phys. Rev. Lett.* **90**, 186602 (2003).

- [13] A. Brataas, Yu. V. Nazarov, and G. E. W. Bauer, *Phys. Rev. Lett.* **84**, 2481 (2000); D. H. Hernando, Yu. V. Nazarov, A. Brataas, and G. E. W. Bauer, *Phys. Rev. B* **62**, 5700 (2000); A. Brataas, Y.V. Nazarov and G.E.W. Bauer, *Eur. Phys. J. B* **22**, 99 (2001).
- [14] T. Tokuyasu, J. A. Sauls, and D. Rainer, *Phys. Rev. B* **38**, 8823 (1988); A. Millis, D. Rainer, and J. A. Sauls, *Phys. Rev. B* **38**, 4504 (1988); M. Fogelström, *Phys. Rev. B* **62**, 11812 (2000); J.C. Cuevas and M. Fogelström, *Phys. Rev. B* **64**, 104502 (2001); N.M. Chtchelkatchev, W. Belzig, Yu.V. Nazarov, and C. Bruder, *JETP Lett.* **74**, 323 (2001); D. Huertas-Hernando, Yu. V. Nazarov, and W. Belzig, *Phys. Rev. Lett.* **88**, 047003 (2002); J. Kopu, M. Eschrig, J. C. Cuevas, and M. Fogelström, *Phys. Rev. B* **69**, 094501 (2004); E. Zhao, T. Löfwander, and J. A. Sauls, *Phys. Rev. B* **70**, 134510 (2004); A. Cottet and W. Belzig, *Phys. Rev. B* **72**, 180503 (2005).
- [15] W. Wetzels, G. E. W. Bauer, and M. Grifoni, *Phys. Rev. B* **72**, 020407 (R) (2005).
- [16] A. Cottet and M.-S. Choi, cond-mat/0605264.
- [17] L. Balents and R. Egger, *Phys. Rev. Lett.* **85**, 3464 (2000); *Phys. Rev. B* **64**, 035310 (2001).
- [18] A. Cottet, T. Kontos, W. Belzig, C. Schönberger and C. Bruder, *Europhys. Lett.* **74**, 320 (2006).
- [19] A. Bachtold, C. Strunk, J.-P. Salvetat, J.-M. Bonard, L. Forro, T. Nussbaumer, and C. Schönberger, *Nature* **397**, 673 (1999); B. Bourlon, C. Miko, L. Forro, D. C. Glattli, and A. Bachtold, *Phys. Rev. Lett.* **93**, 176806 (2004).
- [20] R. Saito, M. Fujita, G. Dresselhaus and M.S. Dresselhaus, *Appl. Phys. Lett.* **60**, 2204 (1992).
- [21] A. De Martino and R. Egger, *J. Phys. Cond. Matter* **17**, 5523 (2005).
- [22] M. Krüger, M. R. Buitelaar, T. Nussbaumer and C. Schönberger, *Appl. Phys. Lett.* **78**, 1291 (2001); M. Krüger, I. Widmer, T. Nussbaumer, M. Buitelaar and C. Schönberger, *New J. Phys.* **5**, 138 (2003).
- [23] J. Barnas and A. Fert, *Phys. Rev. Lett.* **80**, 1058 (1998); A. Braatas, Yu. V. Nazarov, J. Inoue and G. E. W. Bauer, *Phys. Rev. B* **59**, 93 (1999); H. Imamura, S. Takahashi and S. Maekawa, *Phys. Rev. B* **59**, 6017 (1999).
- [24] I. Weymann, J. König, J. Martinek, J. Barnas, and G. Schön, *Phys. Rev. B* **72**, 115334 (2005).
- [25] J. König and J. Martinek, *Phys. Rev. Lett.* **90**, 166602 (2003); M. Braun, J. König and J. Martinek, *Phys. Rev. B* **70**, 195345 (2004); J. König, J. Martinek, J. Barnas, and G. Schön, in "CFN Lectures on Functional Nanostructures", Eds. K. Busch et al., *Lecture Notes in Physics*, Springer, **658**, 145 (2005).
- [26] N. Sergueev, Q.-F. Sun, H. Guo, B. G. Wang, and J. Wang, *Phys. Rev. B* **65**, 165303 (2002); P. Zhang, Q.-K. Xue, Y. Wang, and X. C. Xie, *Phys. Rev. Lett.* **89**, 286803 (2002); R. López and D. Sánchez, *Phys. Rev. Lett.* **90**, 116602 (2003); C. J. Gazza, M. E. Torio, and J. A. Riera, *Phys. Rev. B* **73**, 193108 (2006);
- [27] J. Martinek, Y. Utsumi, H. Imamura, J. Barnas, S. Maekawa, J. König, and G. Schön, *Phys. Rev. Lett.* **91**, 127203 (2003); J. Martinek, M. Sindel, L. Borda, J. Barnas, J. König, G. Schön, and J. von Delft, *Phys. Rev. Lett.* **91**, 247202 (2003); M.-S. Choi, D. Sánchez, and R. López, *Phys. Rev. Lett.* **92**, 056601 (2004); Y. Utsumi, J. Martinek, G. Schön, H. Imamura, and S. Maekawa, *Phys. Rev. B* **71**, 245116 (2005); J. Martinek, M. Sindel, L. Borda, J. Barnas, R. Bulla, J. König, G. Schön, S. Maekawa, and J. von Delft, *Phys. Rev. B* **72**, 121302 (2005); R. Swirkowicz, M. Wilczynski and J. Barnas, *J. Phys. Cond. Matter* **18**, 2291 (2006); R. Swirkowicz, M. Wilczynski, M. Wawrzyniak, and J. Barnas, *Phys. Rev. B* **73**, 193312 (2006).
- [28] B. R. Bulka, *Phys. Rev. B* **62**, 1186 (2000); A. Cottet, W. Belzig, and C. Bruder, *Phys. Rev. Lett.* **92**, 206801 (2004); *Phys. Rev. B* **70**, 115315 (2004).
- [29] S. Sahoo, T. Kontos, J. Furer, C. Hoffmann, M. Gräber, A. Cottet and C. Schönberger, *Nature Phys.* **1**, 99 (2005).
- [30] Y. Meir and N.S. Wingreen, *Phys. Rev. Lett.* **68**, 2512 (1992).
- [31] Y. Meir, N.S. Wingreen and P.A. Lee, *Phys. Rev. Lett.* **66**, 3048 (1991).
- [32] I.L. Aleiner, P.W. Brouwer and L.I. Glazman, *Phys. Rep.* **358**, 309 (2002).
- [33] A. Pasupathy, R. C. Bialczak, J. Martinek, J. E. Grose, L. A. K. Donev, P. L. McEuen, and D. C.

- Ralph, *Science* **306**, 86 (2004).
- [34] J. Nygard, D. H. Cobden, P. E. Lindelof, *Nature* **408**, 342 (2000); M. R. Buitelaar, A. Bachtold, T. Nussbaumer, M. Iqbal, and C. Schönenberger, *Phys. Rev. Lett.* **88**, 156801 (2002); M. R. Buitelaar, T. Nussbaumer, and C. Schönenberger, *Phys. Rev. Lett.* **89**, 256801 (2002); W. Liang, M. Bockrath, and H. Park, *Phys. Rev. Lett.* **88**, 126801 (2002); B. Babic, T. Kontos, and C. Schönenberger, *Phys. Rev. B* **70**, 235419 (2004).
- [35] Z. Yao, H. W. Ch. Postma, L. Balents, C. Dekker, *Nature* **402**, 273 (1999).
- [36] M. Bockrath, D. H. Cobden, J. Lu, A.G. Rinzler, R.E. Smalley, L. Balents, and P.L. McEuen, *Nature* **397**, 598 (1999);
- [37] O. M. Auslaender, H. Steinberg, A. Yacoby, Y. Tserkovnyak, B. I. Halperin, K. W. Baldwin, L. N. Pfeiffer, and K. W. West, *Science* **308**, 88 (2005).
- [38] C.S. Peça and L. Balents, *Phys. Rev. B* **68**, 205423 (2003).
- [39] I. Zutic, J. Fabian and S. Das Sarma, *Rev. Mod. Phys.* **76**, 323 (2004).
- [40] G. Schmidt, D. Ferrand, L. W. Molenkamp, A. T. Filip, and B. J. van Wees, *Phys. Rev. B* **62**, 4790(R) (2000).
- [41] E.I. Rashba, *Phys. Rev. B* **62**, R16267 (2000).
- [42] A. Fert and H. Jaffrès, *Phys. Rev. B* **64**, 184420 (2001).
- [43] C.-M. Hu and T. Matsuyama, *Phys. Rev. Lett.* **87**, 066803 (1998).
- [44] X. Hao, J. S. Moodera, and R. Meservey, *Phys. Rev. B* **42** 8235 (1990); M. Gajek, M. Bibes, A. Barthlmy, K. Bouzehouane, S. Fusil, M. Varela, J. Fontcuberta, and A. Fert, *Phys. Rev. B* **72**, 020406(R) (2005).
- [45] A. Beryazdin, A.R.M. Verschuere, S.J. Tans and C. Dekker *Phys. Rev. Lett.* **80**, 4036 (1998).
- [46] B. Gao, Y. F. Chen, M. S. Fuhrer, D. C. Glattli and A. Bachtold, *Phys. Rev. Lett.* **95**, 196802 (2005).
- [47] J.R. Kim, H.M. So, J.J. Kim and J. Kim, *Phys. Rev. B* **66**, 233401 (2002).
- [48] N. Tombros, S.J. van der Molen and B.J. van Wees, *Phys. Rev. B* **73**, 233403 (2006).
- [49] K. Tsukagoshi, B.W. Alphenaar and H. Ago, *Nature* **401**, 572 (1999).
- [50] K. Tsukagoshi and B.W. Alphenaar, *Superlatt. and Microstr.*, **27**, 565 (2000).
- [51] B. Zhao, I. Mönch, T. Mühl, H. Vinzelberg and C. M. Schneider, *J. Appl. Phys.* **91**, 7026 (2002).
- [52] J. Kong, N.R. Franklin, C. Zhou, M. G. Chapline, S.Peng, K. Cho, and H. Dai, *Science* **287**, 622 (2000); P. G. Collins, K. Bradley, M. Ishigami, and A. Zettl, *Science* **287**, 1801 (2000); S.-H. Jhi, S. G. Louie, and M. L. Cohen, *Phys. Rev. Lett.* **85**, 1710 (2000).
- [53] W. Kim, A. Javey, O. Vermesh, Q.Wang, Y. Li, H. Dai, *Nano Lett.* **3**, 193 (2003).
- [54] A. Jensen, J.R. Hauptmann, J. Nygård and P.E. Lindelof, *Phys. Rev. B* **72**, 035419 (2005).
- [55] A. Jensen, PhD thesis, Technical University of Denmark, Copenhagen (2003).
- [56] B. Nagabhirava, T. Bansal, G.U. Sumanasekera, B.W. Alphenaar and L. Liu, *Appl. Phys. Lett.* **88**, 023503 (2006).
- [57] H.T. Man, I.J.W. Wever and A.F. Morpurgo, *Phys. Rev. B* **73**, 241401(R) (2006).
- [58] S. Sahoo, T. Kontos, C. Schönenberger and C. Suergers, *Appl. Phys. Lett.* **86**, 112109 (2005).
- [59] A. Javey, J. Guo, Q. Wang, M. Lundstrom, and H. Dai, *Nature* **424**, 654 (2003). See also B. Babic, T. Kontos and C. Schönenberger, *Phys. Rev. B* **70**, 235419 (2004).
- [60] L.E. Hueso, J.M. Pruneda, V. Ferrari, G. Burnell, J.P. Valdés-Herrera, B.D. Simmons, P.B. Littlewood, E. Artacho and N.D. Mathur *preprint cond-mat/0511697*.
- [61] J. Wunderlich, T. Jungwirth, B. Kaestner, A. C. Irvine, K. Wang, N. Stone, U. Rana, A. D. Giddings, A. B. Shick, C. T. Foxon, R. P. Campion, D. A. Williams, and B. L. Gallagher, *preprint Phys. Rev. Lett.* **97**, 077201 (2006).
- [62] L. Meier, G. Salis, C. Ellenberger, K. Ensslin, and E. Gini, *Appl. Phys. Lett.* **88**, 172501 (2006).
- [63] H. Shimada, K. Ono, and Y. Ootuka, *J. Phys. Soc. Japan* **67**, 1359 (1997); K. Ono, H. Shimada and Y. Ootuka, *J. Phys. Soc. Japan* **67**, 2852 (1998).
- [64] S.J. van der Molen, N. Tombros, and B.J. van Wees, *Phys. Rev. B* **73**, 220406(R) (2006).
- [65] M. R. Buitelaar, A. Bachtold, T. Nussbaumer, M. Iqbal and C. Schönenberger, *Phys. Rev. Lett.*

- 88**, 156801 (2002).
- [66] S. Sahoo, *PhD thesis*, University of Basel, Basel (2005).
- [67] F. J. Jedema, H. B. Heersche, A. T. Filip, J. J. A. Baselmans, and B. J. van Wees *Nature* **416**, 713 (2002).
- [68] A. Bachtold, M. de Jonge, K. Grove-Rasmussen, P.L. McEuen, M. Buitelaar and C. Schönenberger, *Phys. Rev. Lett.* **87**, 166801 (2001).
- [69] F. Beneu and P. Monod, *Phys. Rev. B* **18**, 2422 (1978).
- [70] F. J. Jedema, A. T. Filip and B. J. van Wees, *Nature* **410**, 345 (2001).
- [71] A.V. Khaetskii and Y.V. Nazarov, *Phys. Rev. B* **61**, 12639 (2000).
- [72] Y.G. Semenov, K.W. Kim and G.J. Iafrate, *preprint*, Cond-mat 0602425.
- [73] T. Ando, *J. Phys. Soc. Japan* **69**, 1757 (2000).
- [74] P. Petit, E. Jouguelet, J.E. Fischer, A.G. Rinzler and R.E. Smalley, *Phys. Rev. B* **56**, 9275 (1997).
- [75] S. Bandow, S. Asaka, X. Zhao and Y. Ando *Appl. Phys. A* **67**, 23 (1998); A.S. Claye, N. M. Nemes, A. Jánossy and J.E. Fischer, *Phys. Rev. B* **62**, R4845 (2000); K. Shen, D.L. Tierney and T. Pietraß, *Phys. Rev. B* **68**, 165418 (2003); J.-P. Salvetat, T. Fehér, C. L’Huillier, F. Beneu and L. Forró, *Phys. Rev. B* **72**, 075440 (2005).
- [76] I. Zutic and M. Fuhrer *Nature Phys.*, **1**, 85 (2005)

This figure "figure7gg.gif" is available in "gif" format from:

<http://arxiv.org/ps/cond-mat/0703472v1>

This figure "figure10.gif" is available in "gif" format from:

<http://arxiv.org/ps/cond-mat/0703472v1>

This figure "figure11.gif" is available in "gif" format from:

<http://arxiv.org/ps/cond-mat/0703472v1>

This figure "figure13a.gif" is available in "gif" format from:

<http://arxiv.org/ps/cond-mat/0703472v1>